Effect of fiber dosage and prestress level on shear behavior of hybrid GFRP-steel reinforced concrete I-shape beams without stirrups

Fatemeh Soltanzadeh*, Ali Edalat-Behbahani, Joaquim A.O. Barros, Hadi Mazaheripour

ISISE, Dep. Civil Eng., School Eng., University of Minho, Campus de Azurém 4800-058 Guimarães, Portugal

ABSTRACT

Corrosion of steel reinforcements embedded in concrete elements is generally known as one of the most common reasons that shorten the service life of the structures. The present study aims to contribute in overcoming this problem by replacing steel stirrups as shear reinforcement of concrete beams using a steel fiber reinforced self-compacting concrete (SFRSCC). In the present research the potential of SFRSCC for improving the shear resistance of the beams without stirrups is explored. In order to further reduce the risk of corrosion in this type of beams, a hybrid system of flexural reinforcement composed of a steel strand and GFRP rebars is applied and properly arranged in order to assure a relatively thick concrete cover for the steel reinforcement. The GFRP bars are placed with the minimum cover thickness for providing the maximum internal arm and, consequently, mobilizing efficiently their relatively high tensile strength. The effectiveness of applying different dosages of steel fibers and varying the prestress force to improve the shear behavior of the designed beam are evaluated. By considering the obtained experimental results, the predictive performance of a constitutive model (plastic-damage multidirectional fixed smeared crack model) implemented in a FEM-based computer program, as well as the one from three analytical formulations for estimating shear resistance of the developed beams were assessed. The FEM-based simulations have provided a good prediction of the deformational response and cracking behavior of the tested beams. All the analytical formulations demonstrated acceptable accuracy for design purposes, but the one proposed by CEB-FIP Modal Code 2010 predicts more conservative shear resistance.

Keywords: Fiber; Hybrid; Mechanical testing, Finite element analysis.

*Author to whom the correspondence should be sent (soltanzadehfaranak@gmail.com).

1. Introduction

Although concrete is a structural material capable of withstanding the aggressive environmental conditions, several reinforced concrete, RC, structures have a premature collapse due to corrosion of their steel reinforcements (Böhni [1]). Corrosion of steel stirrups is one of the most common causes that limits the long-term performance of RC structures, since these conventional shear reinforcements are generally placed with the closest proximity to the exterior surface of the elements. Even seismic safety of the RC structures can be significantly reduced by the premature corrosion of the steel stirrups (Martinelli and Erduran [2]). Hence, finding a method capable of substituting the conventional shear reinforcement is a relatively recent challenge of the scientific community. Beside the risk of corrosion, application of stirrups increases the construction time and cost (Voo et al. [3]). On the other hand, reducing the requirement of stirrups in fabrication of structures offers the possibility of decreasing the elements thickness and structural self-weight, with the derived global benefits. Hence, introducing a strategy to avoid the application of stirrups can contribute for the competitiveness of the precast industry. Available researches (Meda et al. [4], Kwak et al. [5]) argued that steel fibers can substitute partially, or even totally, the conventional shear reinforcements, depending on the applied dosage of steel fibers. These experimental evidences confirmed the significant effect of steel fibers in enhancing the concrete shear behavior (Cuenca and Serna [6], Barragan et al. [7]). Results of these studies demonstrated the efficiency of steel fibers as shear reinforcement to increase the ultimate shear capacity and ductility of the structural elements (Cuenca and Serna [8]). The steel fibers also contribute to reduce the width and spacing of shear cracks, therefore improving the concrete durability and the load carrying capacity of elements at serviceability limit state (Meda et al. [4], Barros et al. [9], Cucchiara et al. [10], Brandt [11]).

Corrosion of the steel flexural reinforcement is another responsible for deterioration and damage process in RC structures (Acciai et al. [12]). Fiber reinforced polymers, FRPs, are alternative flexural reinforcement solutions for the development of durable RC structures, due to their nature and high strength-to-weight ratio (Marí et al. [13], Kara [14]). However, FRPs have a relatively low modulus of elasticity in comparison with that of steel reinforcements. FRP reinforced concrete beams have larger deflection and wider cracks compared to that of steel reinforced concrete elements (Mota et al. [15]). Moreover, the FRP reinforced concrete structures exhibit a brittle failure, and the bond performance between the FRP reinforcements and concrete is normally lower than that of the conventional steel bars and concrete (Achilides and Pilakoutas [16], Mazaheripour et al. [17]). To address these problems, application of steel bars as an additional reinforcement is suggested, resulting in the development of a hybrid system of reinforcement (Aiello and Ombres [18], Yinghao and Yong [19]). This system also offers lower cost constructions than that of the FRP reinforced elements together with the longer service life compared to that of steel reinforced concrete elements (Qu. et al. [20]).

The present study aims to propose a new design methodology for the development of more durable and structurally effective prefabricated concrete beams, taking into account the abovementioned techniques for enhancing the durability of concrete structures (i.e. elimination of stirrups using steel fibers for shear reinforcement, and application of hybrid FRP-steel system for flexural reinforcement). For the fabrication of these elements two designed steel fiber reinforced self compacting concrete, SFRSCC, compositions (with 90 and 120 kg/m^3 steel fibers) of high shear resistance and high compressive strength were developed in an attempt of eliminating the necessity of using steel stirrups as shear reinforcement. The effectiveness of the developed SFRSCC on the shear resistance of the fabricated beams was compared with that of the reference high strength self compacting concrete, SCC, beams with and without conventional stirrups. The beams were flexurally reinforced by employing a hybrid system of a steel strand and glass fiber reinforced polymer, GFRP, bars, being the steel strand positioned with a relatively thick concrete cover for providing proper protection against corrosion, while the GFRP bars are placed near the outer surface of the tensile zone with the highest possible internal arm considering the limitations imposed by the bond performance of these bars (Mazaheripour et al. [17], Mazaheripour et al. [21], Soltanzadeh et al. [22]). The effect of prestressing the GFRP bars on increasing the shear resistance of the SFRSCC elements developed according to the introduced strategy was assessed in previous studies (Soltanzadeh et al. [23], Soltanzadeh et al. [24]). Results of these studies demonstrated that prestressing the GFRP bars contributes to obviate the deficiencies created by the relatively low modulus of elasticity of GFRP. It also helps to control the crack width and improve the shear capacity and mode of failure of FRC elements. In the present study the influence of the prestress level applied to the steel reinforcements, as well as the use of distinct dosages of steel fibers for improving the shear behavior of the developed SFRSCC beams was investigated by testing seven almost real-scale I cross section beams. The behavior of the developed beams is further investigated by means of an advance numerical model implemented in FEM-based computer program. Predictions of the numerical model are presented in terms of deformational and cracking behavior of the beams, as well as the strain field in the reinforcements (GFRP bars, steel strand, and stirrups), having the relevant numerical and experimental results been compared and discussed.

Due to the contribution of steel fibers in concrete shear resistance, the accurate evaluation of the shear capacity of steel fiber reinforced concrete (SFRC) beams is still a challenge. Hence, most of guidelines do not support the total replacement of stirrups by steel fibers (ACI 544.1R-96 [25], Eurocode 2 [26]) in fabrication of SFRC beams. Even some guidelines do not have a design framework to simulate the contribution of steel fibers for the shear capacity of FRC structures (ACI 318-11 [27]). Some guidelines, such as CEB-FIP Model Code 2010 (MC2010) [28] and RILEM TC-162-TDF [29], have already considered the influence of fiber contribution for predicting the shear resistance of SFRC elements. In addition to these guidelines, some formulas have been proposed by researchers, taking into account the effect of steel fibers (Soetens [30], Khuntia et l. [31], Ashour et al. [32], Narayanan and Darwish [33]). In the present research, the predictive performance of MC2010 [28], and RILEM TC-162-TDF [29] guidelines, and the approach proposed by Soetens [30], is assessed by considering the results obtained in the experimental program carried out in the present study.

2. Materials and methods

2.1 Concrete mix design

Based on a mix design methodology proposed by Soltanzadeh et al. [34] for developing self compacting concrete with relatively high dosage of steel fibers, a reference self compacting concrete, SCC, without steel fibers, and two steel fiber reinforced self compacting concrete, SFRSCC, compositions with respectively 90 kg/m^3 (corresponding to the volume fraction, V_f , of 1.1%) and 120 kg/m^3 (V_f = 1.5%) hooked end steel fibers were developed. The adopted steel fibers were 33 mm in length, l_f , and have aspect ratio, l_f / d_f , of 65, and tensile strength of 1100 MPa. A nominal slump flow of about 660 mm was obtained by testing the flowability of the plain SCC and both the SFRSCC mixes according to the slump test (BS EN 12350-8 [35]). In order to have a reliable comparison between the mechanical properties of the concrete mixes at harden stage, all the compositions were designed to pertain to the C50 strength class (MC2010 [28]). The performance of concrete mixes at fresh stage was chosen to obtain the self-compacting requisites along with the mechanical properties suitable for the prefabrication industry at harden stage. The concrete mixes were produced using cement CEM II 52.5R, limestone filler and fly ash class F. Three types of aggregates, containing fine and coarse sand and crushed granite, respectively, with maximum size of 2.4 mm, 4.8 mm and 12.5 mm, were adopted to design the granular skeleton of the mixes. A second-generation of superplasticizer based on polycarboxylate ether (PCE) polymers and water were applied for providing the flowability of the three developed mixes. The SCC and SFRSCC compositions were tailored using 3 kg/m^3 synthetic polyolefin-based macro fibers of 54 mm length and 450 MPa tensile strength. This fiber reinforcement mainly contributes to avoid early plastic shrinkage cracking, and to increase the cohesiveness of the concrete, since the low Young's modulus of these fibers is close to the Young's modulus of concrete in the first hours of hydration (setting hours) (Alberti et al. [36]). The previous studies also confirmed the efficiency of this type of synthetic fibers to increase the concrete fracture energy and toughness at harden state in comparison with that of the ordinary concrete (Alberti et al. [36], Alberti et al. [37]). Table-1 presents the adopted compositions of the three concrete mixes, being nominated by "SCC-F*i*" label, where "*i*" indicates the volume fraction of the steel fibers in the mix.

2.2 Mechanical characterization of the developed concrete mixes

The evaluation of the mechanical performance of the three developed concrete mixes was based on the assessment of the Young's modulus (BS EN 12390-13 [38]) and the compressive (ASTM C39 / C39M - 14a [39]) and flexural (MC2010 [28]) behavior of hardened concretes at the age of 28 days. The average values of the Young's modulus, E_{cm}, and compressive strength, f_{cm}, of SCC-F0 concrete mix, and the two SFRSCC mixes with different dosages of steel fibers, SCC-F1.1 and SCC-F1.5, were tested using nine concrete cylindrical specimens (three specimens per each mix) of 150 mm diameter and 300 mm height. For the SCC-F0 concrete cylinders, the $E_{cm} = 32.10$ GPa (corresponding to the coefficient of variation, CoV, of 2.07%) and $f_{cm} = 66.45$ MPa (CoV = 1.29%) were obtained. For SCC-F1.1 specimens the $E_{cm} = 33.23$ GPa (CoV = 1.15%) and $f_{cm} = 67.05$ MPa (CoV = 1.31%) were determined, whereas the average values of Young's modulus and compressive strength were calculated as $E_{cm} = 30.38$ GPa (CoV = 1.58%) and $f_{cm} = 60.03$ MPa (CoV = 1.94%) for the SCC-F1.5 specimens. These results show a higher average compressive strength for the developed SCC-F0 concrete compared to that of the SFRSCC mix with 120 kg/m^3 steel fibers, SCC-F1.5. It can be attributed to a decrease of 15% of coarse aggregate volume and an increase of 14% the paste volume in the SCC-F1.5 mix compared to that of the mix SCC-F0 in order to ensure a proper flowability and avoiding the perturbation effect of 120 kg/m^3 steel fiber used for tailoring the SCC-F1.5 concrete mix. Since the coarse aggregate is one of the most effective constituent on the concrete compressive strength, which is regarded as the concrete skeleton (Pereira et al. [40]), reducing the volume of coarse aggregate resulted in the reduction of the concrete compressive strength (Chen and Liu [41]). The lower compressive strength of SCC-F1.5 concrete compared to that of the two other developed concrete mixes can also be due to the higher perturbation in the skeleton organization of SCC-F1.5 mix by using the higher content of steel fibers.

The flexural behavior of the SCC and the two SFRSCC mixes at 28 days age was obtained by testing three notched beams per each mix, with a 150×150 mm^2 cross section and 600 mm length under three point loading conditions, following the recommendations of MC2010 [28]. Nominal flexural stress, σ_f, (the $\sigma_f = 1.5PL/(b \times h_{sp}^2)$, where P is the applied load, and b and h_{sp} is the width and depth of the net notched cross section of the specimens) versus crack mouth opening displacement, CMOD, relationship of SFRSCC prisms (developed with SCC-F1.1 and SCC-F1.5 mixes) are presented in Fig. 1 and compared with that obtained by testing the plain SCC prismatic elements (produced by SCC-F0 reference composition). This figure shows that the specimens produced by SCC-F0 concrete mix have a much lower post-cracking flexural capacity than the specimens of the fibrous compositions, SCC-F1.1 and SCC-F1.5. In fact, after visible crack initiation of the matrix (at about 5 MPa), the fiber reinforcement in SCC-F1.1 and SCC-F1.5 assured a significant increase of the flexural capacity (about 3 times), with a very ductile post-peak stage up to 4 mm of CMOD. The residual flexural strength of the specimens produced by SCC-F1.1 mix has exceeded 15 MPa up to the crack width of about 1.5 mm, while this performance was even 13% higher in the SCC-F1.5 concrete specimens with $\sigma_f = 17$ MPa up to reaching 1.5 mm crack width. At a crack width of 3.5 mm the SCC-F1.1 and SCC-F1.5 concrete specimens still developed an average flexural capacity of about 13 MPa and 14 MPa, respectively. By taking the characteristic values of the residual flexural strength parameter at 0.5 mm (f_{R1k}) and at 2.5 mm (f_{R3k}), and considering the recommendations of the MC2010 [28] for the toughness classification of FRC, the SCC-F1.1 and SCC-F1.5 concrete compositions are respectively classified as "13c" and "15c" toughness class. Table-2 represents the stress at the limit of proportionality, $f_{ct,L}^{f}$, (related to the maximum load reached up to CMOD of 0.05 mm) and the values of residual flexural tensile strength, f_{R1} to f_{R4}, (corresponding to distinct values of crack mouth opening displacements, CMOD$_j$, (j=1-4)).

2.3 I-shape beams

Seven quasi-real scale I cross section beams of 4000 mm total length, L, and 500 mm cross section height, h, were designed, fabricated and studied in terms of shear resistance and load carrying capacity in two groups with, respectively, three and four members. The cross sectional dimensions and arrangement of the reinforcements of the beams in both the first and second group is illustrated in Fig. 2. The members of both groups shared the same configuration and geometry, but featured different level of prestress (in the first group of beams with three members) and fiber volume fraction (in the second group of beams with four members). Two different shear spans, of 1475 mm and 1650 mm, were also adopted, respectively, for the beams of first and second group, as shown in Fig. 2. The influence of prestressing the steel longitudinal reinforcements on the shear behavior of the beams was studied by testing the three beams of the first group, while the four beams of second group were tested to investigate the effect of fiber dosage on improving the shear resistance of the developed elements.

The beams in both groups were longitudinally reinforced with one steel strand (15.2 mm diameter with a nominal cross section of 140 mm^2) of seven wires (of 5 mm diameter each, $\phi 5$), and 2 GFRP rebars of 12 mm diameter, $\phi 12$, with ribbed surface. For each member of the two groups a steel-equivalent internal arm, $d_{s,eq}$, is calculated (and provided in Table-3) according to the Eq. (1) by considering the internal arm, d_s and, d_{GFRP}, and the cross sectional area, A_s and A_{GFRP}, of the steel and the GFRP reinforcements, respectively:

$$d_{s,eq} = \frac{A_s d_s + (E_{GFRP} / E_s) A_{GFRP} d_{GFRP}}{A_s + (E_{GFRP} / E_s) A_{GFRP}} \qquad (1)$$

where E_{GFRP} and E_s are, respectively, the modulus of elasticity of GFRP bar and steel strand.

In the previous studies (Soltanzadeh et al. [23], Soltanzadeh et al. [24]) the effect of prestressing the GFRP bars on the shear resistance of the SFRSCC short-span beams (with a relatively small shear span to steel-equivalent depth ratio, $a/d_{s,eq}$, of 2.2) without stirrups was assessed. Thus, the present research deals with beams of I cross section and of higher $a/d_{s,eq}$. In the beams of the first group the level of prestressing force, solely applied to the steel strand, was the main variable investigated. These beams were developed without conventional steel stirrups by using the concrete composition SCC-F1.1 that includes 90 kg/m^3 steel fibers (equal to 1.1% of the concrete volume). Table-3 presents the relevant characteristics of the beams of the first group, using the following designation: G1-F1.1-S*i*, where "G1" indicates the beam pertains to the first group, "F1.1" represents that the beams were developed with SCC-F1.1 concrete composition, and "*i*" is replaced by the prestress level applied to the steel strand (as a percentage of the nominal yield strength of the strand f_{sy}=1740 MPa). For instance, "G1-F1.1-S46" refers to the SCC-F1.1 concrete beam of the first group, reinforced with a steel strand prestressed at 46% of its nominal tensile strength. In the beams of this first group the two GFRP rebars adopted in each beam were applied without prestress (passive flexural reinforcement).

After evaluating the effect of prestress level (applied to the steel strand) on the shear behavior of the beams in the first group, the beams of the second group were developed with constant level of prestress and different dosage of steel fibers, namely: 0%, 1.1% and 1.5% in volume. By testing the beams of the second group, the behavior of the SFRSCC beams developed by SCC-F1.1 and SCC-F1.5 concrete mixes (one per each mixture), and of the plain SCC-F0 beam reinforced with the designed steel stirrups was compared with the behavior of the SCC control beam without conventional shear reinforcements. Both the steel and GFRP reinforcements of this group of the beams were prestressed, the steel strand at 56% of its tensile strength (974 MPa, since f_{sy} =1740 MPa), while the two GFRP bars were prestressed at 30% of its tensile strength (405 MPa, since $f_{GFRP,u}$ =1350 MPa), in accordance with the results of the previous studies (Soltanzadeh, et al. [23], Soltanzadeh, et al. [24]) and in agreement with the recommendations of Canadian Standard Association, CAN/CSA-S06-06, [42] and ISIS Educational Module [43]. All the beams of the second group are introduced by a label "G2-F*j*-ST" in Table-3, where "G2" refers to the second group of the beams and "*j*" is replaced by the volume fraction of steel fibers in the adopted concrete composition. The letters "ST" in this label shows that the beams are reinforced with stirrups. In the case of the beam developed without conventional steel stirrups, the letters "ST" drop from the label and the beam is introduced by the designation of "G2-F*j*". For instance the SFRSCC beam of second group with fiber volume fraction of 1.5% and no stirrups is identified as "G2-F1.5" in Table-3.

Fig. 2 (b) shows the cross section of the SFRSCC beams with 90 and 120 kg/m^3 steel fibers, respectively G2-F1.1 and G2-F1.5, and the control beam developed with the plain SCC, G2-F0, (Sec.2), as well as the SCC element with steel stirrups, G2-F0-ST, (Sec. 3). The beam G2-F0-ST was reinforced with vertically aligned C-shape steel stirrup of 6 mm diameter, $\phi 6$, with spacing of *s*=130 mm. The steel stirrups had the elastic modulus, E_s, of 200 GPa and yield, f_{sy}, and ultimate tensile strength, f_{su}, of respectively 556 MPa and 682 MPa. The shear reinforcement ratio of this beam ($\rho_{sw} = A_{sw} / b_w.s = 0.31\%$, where A_{sw} is the cross sectional area of a steel stirrup, and b_w =70 mm is the web width of the beam cross section) and the spacing were designed in accordance with EN 1992-1-1 [44] recommendations. The vertical part of the stirrups offers resistance to the opening and sliding of the shear cracks, while the bended ends of the stirrups keep it anchored in the concrete. To facilitate the installation of the stirrups and to ensure their proper arrangements, a longitudinal bar of 10mm diameter, $\phi 10$, (with E_s =200 GPa, f_{sy} = 566 MPa and f_{su} = 661 MPa) was placed at the compressive region of this beam.

From the tensile tests executed on GFRP longitudinal reinforcements (ASTM D7205/D7205M-06 [45]), an average value of 56 GPa was obtained for the elasticity modulus of the applied GFRP bars (Mazaheripour et al. [17]). In contrast with the tensile behavior of the high strength steel strand, the GFRP bar behaves elastically and linearly up to failure. The yielding and ultimate tensile stress of steel strand was, respectively, 1740 and

1917 MPa, while the ultimate tensile strength of GFRP bar was 1350 MPa. The steel strand had a modulus of elasticity of 200 GPa.

The average losses in pre-strain of the reinforcements at the moment of testing the beams (28 days after casting each element) was reported as 13.6% and 9.8% for, respectively, GFRP rebars and steel strand (Mazaheripour [46]). The evaluated loss is considered in the calculation of the prestress level of the reinforcements reported in Table-3.

To explore the shear characteristic of the beams fabricated in accordance with the proposed methodology in the present study (i.e. replacement of conventional stirrups with steel fibers and application of hybrid GFRP-steel system of reinforcement), the reference beam of the first group “G1-F1.1-S0” was designed to be over reinforced by adopting a higher flexural reinforcement ratio compared to the hybrid balanced reinforcement ratio of the GFRP-steel reinforced beams. The actual GFRP reinforcement ratio for the present hybrid reinforcing system is calculated according to the following equation.

$$\rho_{GFRP} = \frac{A_{GFRP}}{b_{GFRP} \, . \, d_{GFRP}} \tag{2}$$

where b_{GFRP} is the width of the area under the tensile force due to the GFRP reinforcement (see Fig. 3 (b)). In a rectangular beam, b_{GFRP} is equal to the width of the beam, *b*. When ρ_{GFRP} is higher than the balanced reinforcement ratio of the beam the shear failure will be the governing mode of failure.

The balanced reinforcement ratio of the developed beams in the present study was obtained based on the force equilibrium, strain compatibility and the rectangular stress block hypothesis (CEB-FIP Modal Code 2010 [28]) for the stress distribution in compressive concrete and the stress in tensile GFRP and steel reinforcements, as well as the contribution of steel fibers in the tensile zone in the ultimate limit state (ULS) (CEB-FIP Modal Code 2010 [28]), as presented in Fig. 3(a). Since the ultimate strain of GFRP reinforcements is much greater than the yield strain of steel bar, it is assumed that the steel strand yields before the rupture of GFRP rebars. Hence, the calculated balanced reinforcement ratio assures the simultaneous occurrence of concrete crushing in compression and tensile rupture of GFRP bars at ultimate state, while the steel flexural reinforcement is already yielded (Grace and Singh [47], Bischoff [48]). Then, in the calculation of the balanced reinforcement ratio of the hybrid GFRP-steel reinforcing system, only GFRP balanced reinforcement ratio, ρ_{fb}, is indicated, and the formula is affected by the presence of steel rebars (Leung and Balendran [49], El-Mihilmy et al. [50]). This ratio can be obtained from the following equation for a rectangular cross section FRC beam with hybrid GFRP-steel system of reinforcement (ACI 440.2R-08 [51], CEB-FIP Modal Code 2010 [28]):

$$\rho_{fb} = \frac{1}{f_{GFRP,u}}\left[\alpha_1\beta_1 f_{cm}\,\frac{\varepsilon_{cu}}{\varepsilon_{cu}+\varepsilon_{GFRP,u}-\varepsilon_{GFRP}^{pre}} - \frac{A_s}{b\,.\,d_{GFRP}}\,f_{sy} - \frac{f_{Ftu}(h-e)}{d_{GFRP}}\right] \tag{3}$$

where $\varepsilon_{GFRP,u}$ is the ultimate strain of GFRP rebars, and ε_{cu} represents the ultimate concrete compressive strain, which is assumed as 0.0035 in the present study. Taking into account the strain applied by the prestress, ε_{GFRP}^{pre}, the effect of prestressing the GFRP rebars on the balanced reinforcement ratio is considered in the formula. The contribution of concrete in compression is accounted in Eq. (3) by means of defining the parameters "α_1" and "β_1", in accordance with ACI Committee 440.2R-08 [51], as follow:

$$\beta_1 = \frac{4\,.\,\varepsilon_c' - \varepsilon_c}{6\,.\,\varepsilon_c' - 2\,.\,\varepsilon_c} \tag{4}$$

$$\alpha_1 = \frac{3.\,\varepsilon_c'.\,\varepsilon_c - \varepsilon_c^2}{3\,.\,\beta_1\,.\,\varepsilon_c'^2} \tag{5}$$

where $\varepsilon_c' = 1.7\,f_{cm}/E_{cm}$ is the strain corresponding to the compressive strength of concrete, f_{cm}, and $\varepsilon_c = \varepsilon_{cu}$ for ULS conditions. The last term of Eq. (3), $f_{Ftu}(h-e)/d_{GFRP}$, considers the effect of steel fibers in tension on balanced reinforcement ratio, where f_{Ftu} represents the post-cracking tensile capacity of FRC at ULS, and can be calculated according to the proposed formula by MC2010 [28] guideline:

$$f_{Ftu} = \frac{f_{R3}}{3} \tag{6}$$

In Eq. (3) "e" is the distance between the top of FRC tensile block to the top fiber of the beam cross section (see Fig. 3) that can be calculated as:

$$e = \frac{c_b \times (\varepsilon_{cu} + \varepsilon_{cr})}{\varepsilon_{cu}} \tag{7}$$

where ε_{cr} is the cracking strain of FRC ($\varepsilon_{cr} = f_{ctm}/E_{cm}$, where f_{ctm} is the mean value of tensile strength of FRC), and c_b is the distance of neutral axis from the top fiber of the beam cross section, that can be calculated as:

$$c_b = \frac{\varepsilon_{cu}}{\varepsilon_{cu} + \varepsilon_{GFRP,u} - \varepsilon_{GFRP}^{pre}} d_{GFRP} \tag{8}$$

Since the beams in the present study were developed with an I-shape cross section, Eq (3) was adapted to take into account the particular geometry of the flanged elements (see Fig. 3(a)):

$$\rho_{fb} = \frac{1}{f_{GFRP,u}\,.\,b_{GFRP}\,.\,d_{GFRP}} \times \left[\alpha_1 \beta_1 (\beta_2 b_f) f_{cm} d_{GFRP} \cdot \frac{\varepsilon_{cu}}{\varepsilon_{cu} + \varepsilon_{GFRP,u} - \varepsilon_{GFRP}^{pre}} - A_s f_{sy} - f_{Ftu}(h-e).b_{st} \right] \tag{9}$$

where b_f is the width of the beam flange and β_2 is the parameter for accounting the particular geometry of the adopted I-shape cross section. If the neutral axis falls within the flange height ($c_b \leq h_1$), β_2 =1, while for $h_1 < c_b \leq h_2$, $\beta_2 = 1-(c_b - h_1)(b_f - b_w)/2b_f h_2$ (Mazaheripour [46]) (see Fig. 3(a)). Since the value of c_b in the beam G1-F1.1-S0, calculated as 59.6 mm, is less than the height of the beam flange ($c_b < h_1$), the value of β_2 is considered as unity in the calculations. In Eq. (9) b_{st} and b_{GFRP} are the width of, respectively, the area under the tensile force due to the fiber reinforcement, F_{st} , and GFRP reinforcement, F_{GFRP} , as shown in Fig. 3 (b). The b_{st} and b_{GFRP} are calculated as, respectively, 101.41 mm and 121.17 mm for the beam G1-F1.1-S0. Using the value of f_{R3} obtained experimentally for the concrete SCC-F1.1 and indicated in Table-2, the tensile stress of FRC, f_{Ftu} , is calculated as 4.7 MPa according to Eq. (6), acting at the distance of 61.8 mm form the top fiber of beam cross section (*e* = 61.8 mm). Finally, the balanced reinforcement ratio for the beam G1-F1.1-S0 was calculated as $\rho_{fb} = 0.07\%$ by means of Eq. (9).

Since the designed value of GFRP reinforcement ratio, $\rho_{GFRP} = 0.4\%$, adopted for the beam G1-F1.1-S0 is higher than the GFRP balanced reinforcement ratio, $\rho_{fb} = 0.07\%$, this beam is over reinforced, suggesting that shear is the governing failure mode of the beam. This GFRP reinforced ratio ($\rho_{GFRP} = 0.4\%$) is also applied for reinforcing the rest of the beams in the present study.

2.4 Test setup and measurements

The test setup adopted for all the beams of the first and second groups are represented in Fig. 2. All the beams were simply supported and tested up to their failure under four-point loading configuration. The applied load,

P, was assured by a servo-controlled hydraulic actuator of ±700 kN. The supports were located at a distance of 150 mm from the ends of the beams. The beams of the first group were tested by adopting a shear span to steel-equivalent depth ratio, $a/d_{s,eq}$, of 3.5, while the beams of the second group were tested with $a/d_{s,eq}$ =3.9. Since the concept of equivalent internal arm of the hybrid flexural reinforcements, $d_{s,eq}$, is used for the evaluation of $a/d_{s,eq}$ values in the interval that promotes the occurrence of shear failure in conventional RC beams were also adopted in the beams of the present work.

Since the adopted steel strand was composed of 7 twisted wires, the direct measurement of the strain variation along the steel strand was not possible, and thus, the strain at midspan of the beams was monitored by installing a strain gauge (SG1) only on the GFRP rebars (see Fig. 2). In order to monitor the strain in the stirrups in the case of the beam G2-F0-ST, four additional strain gauges (SG2 to SG5) were attached at the middle of the stirrups, as represented in Fig. 2 (b).

3. Experimental results and discussion

3.1 Failure modes

Load versus mid-span deflection relationship, $P-\delta$, and crack patterns at the failure of the beams of the first and second group are shown in Fig. 4 (a) and (b), respectively. When compared to the control beam of the first group, G1-F1.1-S0, in the other beams of this group a higher number of cracks was detected, with the tendency to increase with the prestress level applied to the beams. These multiple cracks developed gradually in a stable manner, leading to the increase of the load carrying capacity of the beams, depending on the level of prestress. The diagonal cracks continued to propagate towards the top and bottom of the beams in the first group and caused the yielding of the steel strand and failure of the beams. This type of shear failure which is accompanied by yielding of the longitudinal reinforcements is called as diagonal tension mode of failure (ASCE-ACI Committee 426 [52]).

The beams G2-F0 and G2-F0-ST of the second group also failed by diagonal tension mode of failure. By loading the reference beam of group 2, G2-F0, initially the flexural and diagonal cracks developed, but the diagonal cracks propagated and grown more rapidly due to the absence of shear reinforcement mechanisms for resisting to the quick degeneration of these shear cracks in the critical one, which is followed by an abrupt load decay. The cracking behavior of the G2-F0-ST beam shear reinforced with steel stirrups was characterized by

the development of several inclined cracks, which caused the yielding of the stirrups crossed by the critical one (see Fig. 6). Unlike the beams G2-F0 and G2-F0-ST that were produced without steel fibers, the SFRSCC beams G2-F1.1 and G2-F1.5 developed a more diffuse crack pattern composed initially by flexural cracks, and in later stages of the loading process by diagonal cracks, and finally failed with the propagation of in-plane shear crack at the transition between the bottom flange and the web. This failure mode, which is called as shear-tension failure (ASCE-ACI Committee 426 [52]), was accompanied by the formation of horizontal splitting cracks along the steel strand at the tension zone toward the supports of the beams. However, since the longitudinal reinforcement of G2-F1.1 and G2-F1.5 beams were yielded, it is assumed that both the formed flexural and shear cracks interacted to produce the combined shear-flexural mode of failure in these beams.
The formation of the more diffuse crack pattern in the G2-F1.1 beam, with several potential shear failure cracks, is responsible for the pseudo-plastic plateau in the $P-\delta$ response above a deflection of about 30 mm, which is quite evident in Fig. 4 (b). After initiation and propagation of the diagonal cracks, the G2-F1.5 beam continued to resist higher shear load while more cracks were being formed without significant reduction of the stiffness of the beam response, as is visible in Fig. 4 (b). The critical diagonal crack has then propagated through the flange-web interface up to the support with an abrupt load decay. Comparing the G2-F0-ST beam reinforced with steel stirrups, with those made by SFRSCC it is verified that in the former beam a smaller number of cracks with larger distance were formed, while in the SFRSCC beams, the reinforcement provided by steel fibers is the responsible for the development of larger number of cracks of smaller spacing and width, providing to this beam a higher ductility and energy dissipation in the fracture process.

3.2 Load-deflection relationship

Load versus mid-span deflection relationship, $P-\delta$, of the beams of both groups is represented in Fig. 4 (a). As it was expected all the beams were failed by propagation of a critical shear crack, due to their relatively high flexural capacity. However, since the steel strand was yielded in all the beams with exception of the control beam (G1-F1.1-S0) in the first group, which failed in shear, the shear-flexural failure was the governing failure mode in these beams. The failure of the first group of beams has occurred with a considerable deflection level, much higher than the one corresponding to the serviceability limit states, SLS, condition (L/250=16mm). Comparing $P-\delta$ response of the reference beam in the first group, the G1-F1.1-S0 beam with passive longitudinal reinforcements, with those of the G1-F1.1-S23 and G1-F1.1-S46 beams, it can be concluded that by increasing the prestress level of the steel strand the load carrying capacity at SLS, F_{SLS}, (the load corresponding to the deflection of the beam at SLS) increased about 7% and 18% for G1-F1.1-S23 and G1-F1.1-S46 beams, respectively. Since the final purpose of the present study is the development of prefabricated SFRSCC beams capable of entirely suppressing the conventional steel stirrups, a higher level of prestress is applied for producing the second group of beams to ensure the adequate shear resistance for these elements. Hence, a prestress percentage of 56% for steel strand and 30% for the GFRP bars were adopted for prestressing the beams of the second group. All the beams of the second group also presented a relatively high deflection at failure, which was more than three times the deflection of these beams at SLS. The control beam, G2-F0, presented an abrupt load decay just after the peak load, which occurred for a deflection smaller than of the other beams (at 37 mm). An almost similar F_{SLS} was obtained for the beam G2-F0-ST with conventional shear reinforcement compared to the reference beam, G2-F0, since the stirrups does not affect the load carrying capacity of the beam up to the formation of a critical shear crack. The stirrups made the beam G2-F0-ST capable of sustaining load up to a deflection level that was the highest amongst the tested beams in this group, but as expected it also failed by the formation of a critical shear crack, caused by the rupture of stirrups crossing this crack.

By adopting 90 and 120 kg/m^3 steel fibers as a shear reinforcement in the beams G2-F1.1 and G2-F1.5, respectively, the F_{SLS} has increased about 19% and 22% compared to the control beam, G2-F0. A F_{SLS} of almost 223 kN and 230 kN was obtained in G2-F1.1 and G2-F1.5 beams, respectively, which indicates that this type of beams, with convenient geometric adjustments, can be adopted in pre-fabrication for constituting structural systems of buildings of industrial or commercial activities. G2-F1.1 beam, with 90 kg/m^3 steel fibers, for instance, can constitute the support of pre-stressed slabs of a span length between 12 to 17 m for a live load in the range of 4 to 6 kN/m^2 and 5 kN/m^2 permanent load, which is one of the objectives of the present research project (see Fig. 4). The $P-\delta$ obtained in the tested beams clearly supports the benefits of increasing, as much as possible, the prestress level in both flexural reinforcements (the limits imposed by fatigue behavior should be considered).

Although an almost similar F_{SLS} was obtained by testing the beams G2-F1.1 and G2-F1.5, by using 1.5% instead of 1.1% of fiber volume content has provided an increase of 12% in the maximum load carrying capacity, $F_{\max}$, and an increase of 45% in the deflection corresponding to $F_{\max}$. After peak load, the load carrying capacity of the G2-F1.1 beam started decreasing smoothly, and the maximum deflection when shear failure has occurred was similar in G2-F1.1 and G2-F1.5 beams ($\delta \approx 52$ mm). In comparison with the control beam, the G2-F1.1 and G2-F1.5 beams presented an increase in the maximum load carrying capacity, $F_{\max}$, of, respectively, 14.5% and 28%. The increase of $F_{\max}$ was 21% in the case of the beam reinforced with stirrups, G2-F0-ST, when compared to the control beam, G2-F0. The G2-F1.1 and G2-F1.5 beams presented an increase of about 24% and 28% in the F_{SLS} , respectively, when compared to that of the G2-F0-ST beam. The results also show a negligible difference between the $F_{\max}$ of beams G2-F1.1 (without stirrups), and G2-F0-ST (with conventional stirrups). Table-4 resumes the relevant results obtained in both groups of the tested beams.

In order to compare the shear strength between the members of the first and second group with different $a / d_{s,eq}$ ratio, the shear strength of the beams was normalized using "$V_{nz} = V / (b_w d_{s,eq} \sqrt{f_{cm}})$" formula, in accordance with the recommendation of the American Concrete Institute (ACI) 440.IR-06 [53], where *V* is the shear force corresponding to the beam maximum load capacity. The obtained results are depicted in Table-4. By comparing the normalized shear strength, V_{nz} , of the beams G1-F1.1-S0, G1-F1.1-S23 and G1-F1.1-S46 (respectively equal to 0.501, 0.511 and 0.513 MPa$^{0.5}$) of the first group, with that of the G2-F1.1 beam (V_{nz} =0.550 MPa$^{0.5}$) in the second group, all of them with the same dosage of steel fibers, a significant effect of the prestress level on the increase of the shear strength is verified. Hence, by applying 1.6 MPa, 3.2 MPa and 6.5 MPa prestress in the beams, respectively, G1-F1.1-S23 and G1-F1.1-S46 (by prestressing the strand), and G2-F1.1 (by means of prestressing both the steel strand and GFRP bars), the normalized shear strength has increased 7%, 7.2% and 9.3% compared to the control beam with no prestress, G1-F1.1-S0. The normalized values of shear strength also demonstrate that the beam G2-F0 without any shear reinforcement has presented the lowest V_{nz} , as expected. Comparing the V_{nz} value calculated for the beam G2-F0 with that of the beams G1-F1.1-S0, G1-F1.1-S23 and G1-F1.1-S46 in the first group, it is verified that, in spite of the highest level of prestress applied in the beam G2-F0, the V_{nz} value was higher in the case of the G1-F1.1-S0, G1-F1.1-S23 and G1-F1.1-S46 beams with lower level of prestressed, which evidences the significant effect of steel fibers on improving the shear resistance of the beams. Finally, the V_{nz} of the beam G2-F0-ST, with steel stirrups, was intermediate to the ones of G2-F1.1 and G2-F1.5, reinforced with steel fibers, which indicates the possibility of developing a new generation of hybrid reinforced beam without conventional stirrups of enhanced durability, as long as an adequate SFRC, together with an appropriate level of prestress are considered in the design of these beams.

3.3 Stress-strain response

Variation of strain in the GFRP bars at mid-span of the beams in the first group during the loading process ($P-\varepsilon_{GFRP}$ relationship) is represented in Fig. 5 (a). The results corresponding to the beam G1-F1.1-S46 are not reported in Fig. 5 (a) due to the deficient functioning of the strain gauge installed in this beam. This figure shows that by increasing the prestress level in the steel strand, the tensile strain in the GFRP reinforcement decreases due to the initial compression strain field introduced in the zone of the hybrid flexural reinforcement. In fact, prestressing the steel strand caused a negative curvature (compressive strain in the bottom surface of the beam), with an initial compressive strain in its surrounding concrete. This effect has delayed the crack initiation, causing the fibers to be later activated, which justifies the smaller gradient of strain during the loading process when compared to the G1-F1.1-S0, i.e., at the same level of applied load the strain in GFRP bar of the control beam (G1-F1.1-S0) is higher than that of the beam G1-F1.1-S23, and this tendency has increased during the loading process.

The $P-\varepsilon_{GFRP}$ relationships of the beams of the second group are represented in Fig. 5 (b). This figure evidences that the strain response of the GFRP bars was affected by the dosage of steel fibers adopted for producing the beams. In fact, by increasing the dosage of steel fibers from 0% (adopted in G2-F0 beam) up to 1.5% (applied in G2-F1.5 beam) the strain in GFRP bar has decreased for the same load level applied to the beam. This can be attributed to the tension stiffening effect of the fibers bridging the cracked concrete surrounding the flexural reinforcement, as demonstrated in a previous work (Mazaheripour et al. [54]).

A closer inspection of Fig. 5 (b) reveals that the $P-\varepsilon_{GFRP}$ responses of the beam G2-F0 (the beam with neither stirrups nor steel fibers) and G2-F0-ST (the beam with stirrups but without steel fibers) are very close up to the load ≈ 229 kN, which corresponds to the failure load of the G2-F0 beam. Above this load level, the beam G2-F0-ST demonstrated an increase of the gradient of strain in the GFRP bars, which can be justified by the loss of shear stiffness due to the initiation of significant shear damage, with a consequent increase of the curvature and strains in the flexural reinforcements. Fig. 6 demonstrates that the two monitored stirrups, installed at the shear span in which the critical shear crack was localized, were yielded at the failure stage of the beam G2-F0-ST.

The advantages of applying steel fibers as the shear reinforcement over the application of conventional stirrups can be observed by comparing the $P-\varepsilon_{GFRP}$ response of the beams G2-F0-ST, G2-F1.1 and G2-F1.5. Fig. 5 (b) shows the load at the effective activation of the GFRP bars has significantly increased with the content of fibers, since fibers bridging the micro-cracks of concrete surrounding the GFRP bars have restricted effectively the crack propagation due to the relatively high post-cracking tensile capacity of the developed SFRSCC (see Table-2). This fiber reinforcement effect has also decreased the gradient of strains in the GFRP bars during the loading process.

From the recorded tensile strains, it is clear that the GFRP bars did not reach their ultimate strain and, no one has ruptured, having the normalized maximum tensile strain (divided by the ultimate tensile strain, 2.4%) varied between 32% (in case of beam G1-F1.1-S23) to 93% (in case of beam G2-F0-ST).

4. Finite element analysis

4.1 Introduction

The plastic-damage multidirectional fixed smeared crack (PDSC) model available in FEMIX 4.0 computer program (Sena-Cruz et al. [55]) was used in order to assist the interpretation of the behavior of the developed beams. The PDSC model is described in detail elsewhere (Edalat-Behbahani et al. [56]), so only a brief resume of the model is presented in this study. The PDSC model is described at the domain of an integration point (IP) of a plane stress finite element.

4.2 Relevant aspects of the constitutive model

The crack initiation occurs when the maximum principal tensile stress in an IP attains the concrete tensile strength (f_{ct}) under an assumed tolerance. After crack initiation, the relationship between normal stress and normal strain in the crack coordinate system, i.e. $\sigma_n^{cr} - \varepsilon_n^{cr}$, is simulated via the quadrilinear diagram represented in Fig. 7 (a) (Ventura-Gouveia [57]). Normalized strain, $\xi_i \, (i = 1, 2)$, and stress, $\alpha_i \, (i = 1, 2)$, parameters are used to define the transition points between linear segments, being G_f^{I} the fracture energy mode I, while l_b is the characteristic length (crack bandwidth) used to assure that the results of a material nonlinear analysis is not dependent of the refinement of the finite element mesh.

The model simulates the degradation of shear stress transfer during the crack opening process by means of the shear softening diagram represented in Fig. 7 (b). The crack shear stress, τ_t^{cr}, increases linearly with the crack shear strain, γ_t^{cr}, up to attain the crack shear strength, $\tau_{t,p}^{cr}$, (hardening branch), followed by a linear decrease in shear residual stress with the increase of the crack shear strain (softening branch). In Fig. 7 (b) the variable $\gamma_{t,u}^{cr}$ is the ultimate crack shear strain depending on $\tau_{t,p}^{cr}$, shear fracture energy $G_{f,s}$, and l_b (Ventura-Gouveia [57]).

The model assumes plastic flow occurs in the undamaged (undamaged respect to compressive loadings) configuration of the material, therefore the plasticity part of the model is formulated in effective (undamaged respect to compressive loadings) stress space. The nonlinear compressive behavior of the material in effective stress space is governed the law represented in Fig. 7 (c), designated here as hardening function ($\bar{\sigma}_c$) – hardening parameter ($\tilde{\epsilon}_c$) law. The hardening function ($\bar{\sigma}_c$) carries the meaning of current effective uniaxial compressive stress, while the hardening parameter ($\tilde{\epsilon}_c$) is a scalar measure used to characterize the plastic state of the material under compression. In Fig. 7 (c) f_{cm} is the compressive strength, $\tilde{\epsilon}_{c1}$ is hardening parameter at compressive strength, and f_{c0} is the uniaxial compression stress at the initiation of the stress-strain nonlinear behavior, defined by the α_0 that is a material constant in the range $]0,1[$ i.e. $f_{c0} = \bar{\sigma}_c(\tilde{\epsilon}_c = 0) = \alpha_0 f_{cm}$.

Strain softening and the stiffness degradation of the material under compression for the domain $\tilde{\epsilon}_c > \tilde{\epsilon}_{c1}$ is simulated by a damage law. The damage model assumes the state of damage in compression is equally distributed in all the material direction (isotropic damage) and can be represented by the scalar damage variable, d_c, in the range of $[0,1]$. Fig. 7 (d) represents the evolution of the scalar damage variable, d_c, as a function of the hardening parameter, $\tilde{\epsilon}_c$. Analysis of Fig. 7 (d) indicates that at the plastic deformations corresponding to $\tilde{\epsilon}_c \le \tilde{\epsilon}_{c1}$ the material is assumed intact ($d_c = 0$), and for $\tilde{\epsilon}_c = \tilde{\epsilon}_{cu}$ the material is completely damaged ($d_c = 1$). The variable $\tilde{\epsilon}_{cu}$ is the maximum equivalent strain in compression that is dependent of the compressive fracture energy ($G_{f,c}$), the characteristic length for compression (l_c), the compressive strength (f_{cm}), and $\tilde{\epsilon}_{c1}$ (Edalat-Behbahani et al. [56]).

4.3 FEM modelling, results and discussions

Eight-noded serendipity plane stress finite elements with 3×3 Gauss–Legendre IP scheme were used for modeling the beams of both groups 1 and 2. In Fig. 8 is represented, as an example, the finite element mesh used for the simulation of the beam G1-F1.1-S0. The longitudinal steel strand and GFRP bars were modeled using 2-noded cable elements (one degree-of-freedom per each node) with two IPs. The compressive reinforcement and steel stirrups installed in the beam G2-F0-ST are meshed using 2-noded embedded cables with two IPs. Perfect bond was assumed between the reinforcement bars/strand and the surrounding concrete. For modeling the behavior of steel reinforcement, the stress-strain relationship represented in Fig. 7(e) was adopted. The curve (under compressive or tensile loading) is defined by the points PT1 = ($\varepsilon_{sy}, \sigma_{sy}$), PT2 = ($\varepsilon_{sh}, \sigma_{sh}$), and PT3 = ($\varepsilon_{su}, \sigma_{su}$) and a parameter P_s that governs the shape of the last branch of the curve. Unloading and reloading linear branches with slop of $E_s = \sigma_{sy} / \varepsilon_{sy}$ are assumed in the present approach (Sena-Cruz [58]). The values of the parameters that define the stress-strain law (Fig. 7(e)) for the steel strand, stirrups, and compressive reinforcement are included in Table-5. The behavior of GFRP bar was modeled using a linear-elastic stress-strain relationship. The prestress load was simulated by means of temperature variation applied to the cable elements modeling the GFRP bars and steel strand. Table-6 includes the values of the temperature variation applied for each simulated beam. The values of the parameters used to define the constitutive law for concretes SCC-F0, SCC-F1.1 and SCC-F1.5 are indicated in Table-7. To simulate the shear crack initiation and the degradation of crack shear stress transfer, the shear softening diagram represented in Fig. 7 (b) is assumed, and the values of the parameters to define this diagram for each concrete are included in Table-7. Due to lack of reliable experimental evidences to characterize this diagram, the adopted values are indirectly obtained from the test data using the inverse method (by simulating the experimental results as best as possible) (Ventura-Gouveia [57]). For the concretes SCC-F1.1 and SCC-F1.5 the same crack shear strength was used ($\tau_{t,p}^{cr} = 1.75$ MPa), while for the concrete SCC-F0 the value 1.2 MPa was adopted for $\tau_{t,p}^{cr}$. The shear fracture energy for the concrete without steel fiber (concrete SCC-F0) was adopted as $G_{f,s} = 0.08$ N/mm. For the concretes including the steel fibers (concretes SCC-F1.1 and SCC-F1.5) higher values of $G_{f,s}$ are adopted, as indicated in Table-7, to simulate the effect of fiber reinforcement in resisting the degradation of shear stress transfer between the faces of the cracks during the cracking process.

It should be aware that in the approach followed in the current work for modeling the behavior of SFRSCC (i.e. SCC-F1.1, and SCC-F1.5), this material is considered to be homogeneous. However SFRSCC can be regarded as heterogeneous medium, like the approach proposed by Cunha et al. [59]. Within their numerical model, SFRSCC was modeled as a material composed of two phases: matrix and discrete steel fibers. The matrix phase is simulated with 3D multidirectional fixed smeared crack model, while the stress transfer between crack planes due to the reinforcing mechanisms of fibers bridging active cracks is modeled with 3D embedded elements. This approach is, however, too demanding in terms of computer time consuming when applied to elements of structural scale, which is the type of structures analyzed in the present work.

Fig. 9 and Fig. 10 compare the numerical and the experimental load vs. mid-span deflection for the beams of first and second groups, respectively. Fig. 11 represents, as an example, the numerical crack pattern for the simulation of the beams G2-F1.5 at the end of the analysis (at the end of the last converged loading step). The figures 9-11 show that the numerical model is able to capture with good accuracy the deformational response of the beams and the experimentally observed profile of the failure crack. For all the beams the numerical peak load, $F_{\max}^{Num}$, predicted by the model are compared with the experimental ones, $F_{\max}$, in Table-8. The information provided in Table-8 demonstrates the peak loads of all the beams are closely simulated with the average error of 6.07%.

Fig. 12 compares the numerical and the experimental load vs. strain ($P-\varepsilon_{STIRRUP}$) relationship, where strain was registered in the location where the strain gauges SG4 and SG5 were installed in the stirrups of the beam G2-F0-ST. This figure indicates the both stirrups are already yielded at the failure stage of the beam G2-F0-ST, which was also observed in the experimental program. The predicted $P-\varepsilon_{GFRP}$ relationships (load versus strain obtained in the IP closest to the mid-span of the beam) for all the beams, except for the G1-F1.1-S46 beam (due to malfunctioning of the corresponding strain gauge), are compared with those of experiments in Fig. 13. Fig 12 and Fig. 13 show numerical simulations, in general, predict with good accuracy the strain measured in the stirrups and GFRP bars, which means the assumption of perfect bond between the steel stirrups and GFRP bars and surrounding concrete adopted in these simulations is acceptable. It should be aware that strains recorded by strain gauges are quite dependent on their distance to the cracks crossing the reinforcements where they are installed.

The numerical relationships of the load versus the strain of steel strand at the mid-span ($P-\varepsilon_{STRAND}$) for all the developed beams are represented in Fig. 14 (the strain is obtained at the IP closest to the mid-span of the beam). Fig. 14 shows that the steel strand is not yielded in the control beam of the group 1 (the beam G1-F1.1-S0), while in the beams G1-F1.1-S23 and G1-F1.1-S46 (the beams in group 1 and with prestress applied to the steel strand) the steel strand has yielded at the loads about 230 kN.

For the beams G2-F0 and G2-F0-ST, which are in the second group and made by concrete SCC-F0, the steel strands has yielded at the load of about 200 kN. The predicted strain in the strand at failure stage of the beam G2-F0-ST is about 77% higher than that of the G2-F0, which is mainly due to the larger ultimate deflection of the beam G2-F0-ST. For the beams in the second group and made by SFRSCC (the beams G2-F1.1 and G2-F1.5), the yield initiation of steel strands has occurred at the load of about 240 kN. This load is higher than those predicted for the beams made by concrete SCC-F0 (the beams G2-F0 and G2-F0-ST), since the steel fibers bridging the flexural cracks crossing the steel strand have contributed to decrease the average strain installed in the strand (Mazaheripour et al. [54]). Taking into account that the steel strand of the G1-F1.1-S0 beam was the unique to have not yielded, the remaining beams can be considered as having failed in flexural-shear, since the formation of a critical shear crack in these beams has occurred after yield initiation of the steel strand and was caused by the strain-hardening character of this type of steel, and the linear behavior and relatively high ultimate tensile strain of GFRP bars.

5. Shear resistance

The shear resistance of the tested beams in both the first and second group is compared with predicted ones according to the formulations proposed by MC2010 [28], RILEM TC 162-TDF [29], and Soetens [30]. These formulations are resumed in Table-9 (Eq. (10) to (20)), whose detailed description can be found in Soltanzadeh et al. [23].

In accordance with RILEM TC 162-TDF [29] approach, the shear resistance of FRC beams, V_{Rd}, is calculated as follow:

$$V_{Rd} = (V_{cd} + V_{fd}) + V_{wd} \tag{21}$$

where V_{cd}, V_{fd} and V_{wd} are the contribution of concrete, fiber reinforcement, and steel stirrups, respectively. According to the RILEM TC 162-TDF [29] approach, the shear resistance of a FRC beam without stirrups comprises the shear resistance provided by concrete, V_{cd}, (can be calculated according to Eq. (10)) and the shear resistance related to the contribution of steel fiber reinforcement, V_{fd} (can be calculated using Eq. (12)).

To determine the shear resistance of FRC beams, the MC2010 [28] merges the contribution of fiber reinforcement, V_{fd}, and concrete, V_{cd}, in an unique term, $V_{Rd,F}$, (can be calculated according to Eq. (15)) thereby Eq. (21) is reduced to the following equation in accordance with MC2010 [28]:

$$V_{Rd} = V_{Rd,F} + V_{wd} \tag{22}$$

Both RILEM TC 162-TDF [29] and MC2010 [28] guidelines address the contribution of the transversal reinforcement, V_{wd}, in the same way, as represented in Eq. (23).

$$V_{wd} = \frac{A_{sw}}{s} 0.9d \; f_{ywd} (1 + \cot \alpha) \sin \alpha \tag{23}$$

In this formula f_{ywd} is the design value of the yield stress of shear reinforcement, and α is angle formed by this reinforcement with the longitudinal axis of the beams.

The approach proposed by Soetens [30] can be written in the following general form:

$$V_{Soetens2015} = (A\sqrt{f_{cm}} + Bf_{Ftu}^{*})b_w z \tag{24}$$

where $z = 0.9d_{s,eq}$ is internal lever arm of the flexural reinforcement. The first term of Eq. (24) represents the concrete contribution for the shear resistance of the FRC beams. The factor " A " in this term is a function of the parameters assumed as having the highest influence for the reinforced concrete shear resistance, namely the effective depth of the beams, *d*, the longitudinal reinforcement ratio, ρ_s, the shear span to effective depth ratio, *a/d*, and the compressive stress due to the application of prestress, σ_{cp} (see Eq. (19) in Table-9). The second term of Eq. (24) considers the contribution of the fiber reinforcement for the shear resistance of a FRC beam. In this term the ultimate post-cracking tensile strength of FRC, " f_{Ftu}^{*} " should be calculated according to the following equation:

$$f_{Ftu}^{*} = \min \begin{cases} f_{Ftum} \\ f_{ctm}(1 - 2\sigma_{cp} / f_{cm}) \end{cases} \tag{25}$$

where f_{Ftum} is the average ultimate post cracking tensile strength of FRC, and f_{ctm} is the average of its tensile strength.

As it is shown in Table-9, the Soetens [30] formula is only developed for the prediction of shear resistance of FRC beams without steel stirrups.

The shear resistance of the tested beams of the first and second group, $V_{\exp}$, and the corresponding shear strength, $v_u = V_{\exp}/(bd_{s,eq})$ are included in Table-10. The experimental results are compared with the estimated ones according to MC2010 [28], (V_{MC2010}), RILEM TC 162-TDF [29], (V_{RILEM}), and Soetens [30], ($V_{Soetens2015}$), approaches. For the calculations of V_{MC2010}, V_{RILEM} and $V_{Soetens2015}$, average values were considered for the material properties, and the unitary value was taken for the partial safety factor for the material properties "γ_c". The flexural reinforcement ratio, ρ_s, presented in these formulas was replaced by the equivalent steel reinforcement ratio, $\rho_{s,eq}$, determined by Eq. (26) (Qu et al. [20]), since the tested beams in this study were reinforced with hybrid GFRP-steel bars:

$$\rho_{s,eq} = \frac{A_s}{b_w d_s} + \frac{E_{GFRP}}{E_s}\frac{A_{GFRP}}{b_w d_{GFRP}} \tag{26}$$

According to this formula, the equivalent steel reinforcement ratio, $\rho_{s,eq}$, was calculated as 0.24% for all the beams of the present study.

The effective depth, d, in the MC2010 [28], RILEM TC 162-TDF [29] and Soetens [30] approaches was substituted by the equivalent steel depth, $d_{s,eq}$, calculated according to Eq. (1). Comparing the ratio of shear resistance obtained experimentally to the estimated ones by the three considered approaches, it is verified that RILEM TC 162-TDF [29] approach is the one that closest estimates the shear resistance of SFRSCC beams in average terms ($V_{\exp}/V_{RILEM}$ =1.05), but the CoV is relatively high (≈38%). However, RILEM TC 162-TDF [29] approach has underestimated significantly the shear resistance of the beam G2-F0, developed by plain concrete. Hence, if this beam is excluded in the analysis, an average value of 0.91 is obtained for the $V_{\exp}/V_{RILEM}$ with a CoV of about 18%. This demonstrates that the proposed approach has marginally overestimated the shear resistance of the developed prestressed beams with shear reinforcements (i.e. stirrups or steel fibers). In average terms the formula proposed by Soetens [30] provided a smaller underestimation ($V_{\exp}/V_{Soetens2015}$ =1.11), but the too high CoV (≈67%) indicates the inappropriateness of this approach for the beams of plain concrete, G2-F0-ST. In fact, if G2-F0 is excluded from this analysis, the average value of $V_{\exp}/V_{Soetens2015}$ is 0.81 with a CoV of about 6.8%, which indicates the formulation overestimates the shear capacity of FRC beams, but the CoV is relatively small, so it has good potential for design purposes, requiring further improvements on the calibration of the model parameters.

The MC2010 [28] formula provides quite conservative estimations, with an average $V_{\exp}/V_{MC2010}$ of 1.68, but with a relatively low CoV (≈15%). The calculated values according to this approach are, in average terms, 41% lower than the ones calculated by RILEM TC 162-TDF [29] provisions and 44% lower than Soetens [30] formula. Comparison of Eq. (10), proposed by RILEM TC 162-TDF [29], with Eq. (15) recommended by MC2010 [28], shows that the contribution of fibers for the shear resistance in Eq. (15) is only reflected on parameter "$C2$". The shear contribution of fibers in Eq. (15) is modeled by modifying the longitudinal reinforcement ratio (Minelli et al. [60]) through the factor $C2$ that includes a parameter representative the post-cracking performance of FRC at a crack width of 1.5 mm, f_{Ftuk} (see Eq. (16) in Table-9). In order to estimate how the fibers contribution is taken into account according to MC2010 [28] approach, the shear resistance of plain concrete was calculated by means of keeping $C2$=1 (which means f_{Ftuk}=0). Hence, the fiber contribution was evaluated by subtracting the calculated value of the shear resistance for plain concrete from the estimated shear resistance of FRC by Eq. (15). The analytical shear values corresponding to the contribution of concrete, V_{cd}, and fiber reinforcement, V_{fd}, for the shear resistance of all the beams of first and second group in accordance with MC2010 [28] and RILEM TC 162-TDF [29] approaches are indicated in Fig. 15. This figure evidences that the significant difference on the estimation of shear resistance of the beams is related to distinct calculation of V_{fd}. Regarding the values given in Fig. 15, it can be found that RILEM TC 162-TDF [29] formula yields more accurate predictions for the tested beams in this study in comparison with the MC2010 [28] shear model, in terms of the predicted load. Hence, it can be concluded that RILEM TC 162-TDF [29] formula gives more accurate predictions of fiber contribution compared to MC2010 [28] formula, since the contribution of concrete is estimated similarly according to both these guidelines. The contribution of steel fibers for the shear capacity of the beams is estimated 73% lower by MC2010 approach compared to the one calculated according to the RILEM TC 162-TDF [29] formulation. This figure evidences that MC2010 [28] underestimates significantly the contribution of fiber reinforcement for the shear resistance.

In Eq. (19) of the Soetens [30] approach the concrete, V_{cd}, and fiber contribution, V_{fd}, for the shear resistance of the FRC beams are estimated by the functions A and B, respectively, and the obtained values are compared in Fig. 15 to those determined from the RILEM TC 162-TDF [29] and MC2010 [28] approaches. This comparison shows that the Soetens [30] approach predicts the highest contribution of the fiber effects, respectively, 77% and 14% higher than the calculated ones by MC2010 [28] and RILEM TC 162-TDF [29] approaches, when estimating the shear resistance of FRC beams.

6. Conclusions

An experimental program composed of 7 almost full-scale I cross section SFRSCC beams flexurally reinforced with a hybrid system of a steel strand and GFRP rebars was executed for assessing the potentialities of these new types of materials for the development of an innovative structural system almost immune to corrosion. During this research, three types of concrete compositions composed of 0, 90 and 120 kg/m^3 steel fibers, with rheological and mechanical properties suitable for the production of precast prestressed structural elements, were developed and applied for fabrication of the beams. The effectiveness of applying different dosages of steel fibers and distinct levels of prestress for improving the shear behavior of the designed beams without stirrups was assessed experimentally and numerically. Based on the results obtained in the present study, the reliability of the existing analytical approaches for estimating the shear resistance of the beams was investigated as well. From the analysis of the load *vs.* deflection response, strain variation in GFRP rebars, failure mode, as well as crack pattern of the tested beams, the following conclusions can be drawn:

– Prestressing the steel reinforcement provided a confinement in the beams of the first group. This confinement delayed the crack opening and consequently caused the fibers to be later activated. Hence, adopting a prestress level of the steel strand up to 46% of its tensile strength, contributes to enhance the shear resistance of the beam and, consequently, the load carrying capacity was increased 18% at serviceability limit state.

– By adopting the same prestress level for the hybrid flexural reinforcement (56% for the steel strand and 30% for the GFRP bars) the load carrying capacity of the SFRSCC beams without shear reinforcements was increased at least 24% as serviceability limit state compared to the plain concrete beam with conventional shear reinforcements. These SFRSCC beams have presented a very ducktail response and at the failure stage the steel strand was already yielded. The load level and the ductility performance indicate that this type of SFRSCC beams flexurally reinforced with hybrid prestressed reinforcements can be adopted in pre-fabrication for buildings with industrial or commercial activities.

– The similar shear capacity of the developed SFRSCC beams and the one shear reinforced with steel stirrups at ultimate limit state indicates the possibility of developing the concrete structural elements without stirrups by adopting an adequate dosage of steel fiber together with an appropriate level of prestress.

– By comparing the estimated shear resistance of the developed beams in the present study in accordance with MC2010 [28] and RILEM TC 162-TDF [29] as well as the formula proposed by Soetens [30], it is verified that RILEM TC 162-TDF [29] approach provided more accurate predictions. The shear capacity of the beams according to MC2010 [28] was much lower than the one recorded experimentally, indicating the necessity of further research for better tailoring the contribution of fiber reinforcement for the shear capacity of FRC beams.
– A comprehensive life-cycle analysis integrating the direct and indirect costs related to the durability should be executed in the future to assess the comprehensiveness of the developed solution for fabricating reinforced concrete elements.

ACKNOWLEDGEMENTS

The first and second authors, respectively, acknowledge the research grant in the ambit of the project "UrbanCrete", with reference number of 30367, supported by the European Regional Development Fund (FEDER), and "SlabSys-HFRC", with reference PTCD/ECM/120394/2010, supported by the Portuguese Foundation for Science and Technology (FCT). The authors also thank the collaboration of the following companies: Tensacciaci in the name of Eng. F. Pimenta for the assistance on the application of prestress reinforcements, Sireg and Schoeck for providing the GFRP rebars, Casais to manufacture the moulds, Exporplas for supplying the polypropylene fibers, Secil/Unibetão for providing the Cement, BASF for supplying the superplasticizer and CiviTest for collaborating in producing the specimens.

References

[1] Böhni H. Corrosion in reinforced concrete structures, Woodhead, Cambrigd, U.K., 2005.

[2] Martinelli E, Erduean E. Seismic capacity design of RC frames and environment-induced degradation of materials: Any concern?. J Eng Stract 2013; 52: 466-477.

[3] Voo Y, Poon W, Foster S. Shear strength of steel fiber-reinforced ultrahigh- performance concrete beams without stirrups. J Struct Eng 2010; 136(11): 1393-1400.

[4] Meda A, Minelli F, Plizzari GP, Riva P. Shear behavior of steel fiber reinforced concrete beams. J Mater Struct 2005; 38:359-366.

[5] Kwak YK, Eberhard MO, Kim WS, Kim J. Shear strength of fiber/reinforced concrete beams without stirrups. ACI Struct J 2002; 99(4): 530-538.

[6] E. Cuenca, P. Serna, Shear behavior of self-compacting concrete and fiber-reinforced concrete push-off specimens (2010). In: Khayat KH, Feys D (eds.). Design production and placement of self-consolidating concrete, Proceedings of SCC2010, vol. 1. Montreal, Canada: RILEM Bookseries; 2010. p. 429-66.

[7] Barragan B, Gettu R, Agullo L, Zerbino R. Shear failure of steel fiber-reinforced concrete based on push-off tests. ACI Mater J 2005; 103:251-257.

[8] E. Cuenca, P. Serna, Failure modes and shear design of prestressed hollow core slabs made of fiber-reinforced concrete, J Comp. Part B: Eng 2013; 44:952-964. ISSN 1359-8368, pp. 952-964, http://dx.doi.org/10.1016/j.compositeb.2012.06.005.

[9] Barros JAO, Lourenço LAP, Soltanzadeh F, Taheri M. Steel-fiber reinforced concrete for elements failing in bending and in shear. Eur J Environ Civil Eng 2013; 18(1): 33-65.

[10] Cucchiara C, Mendola LL, Papia M. Effectiveness of stirrups and steel fibers as shear reinforcement. Cem Concr Compos J 2004; 26(7):777-786.

[11] Brandt AM. Fiber reinforced cement-based (FRC) composites after over 40 years of development in building and civil engineering. J Compos Struct 2008; 86:3-9.

[12] Acciai A, D'Ambrisi A, De Stefano M, Feo L, Focacci F, Nudo R. Experimental response of FRP reinforced members without transverse reinforcement: Failure modes and design issues. J Compos Part B 2016; 89:397-407.

[13] Marí A, Cladera A, Oller E, Bairán J. Shear design of FRP reinforced concrete beams without transverse reinforcement. J Compos Part B 2014; 57:228-241.

[14] Kara IF, Ashour AF, Köroğlu MA. Flexural behavior of hybrid FRP/steel reinforced concrete beams. J Compos Struct 2015; 129: 111-121.

[15] Mota C, Almiar S, Svecova D. Critical review of deflection formulas for FRC/RC members. J Compos Constr 2006; 10(3):183-194.

[16] Achilides Z, Pilakoutas K. Bond behavior of fiber reinforced polymer bars under direct pullout condition. J Compos Constr 2004; 8(2): 173-181.

[17] Mazaheripour H, Barros JAO, Sena-Cruz JM, Pepe M, Martinelli E. Experimental study on bond performance of GFRP bars in self-compacting steel fiber reinforced concrete. J Compos Struct 2013; 95: 202-212.

[18] Aiello MA, Ombres L. Structural performances of concrete beams with hybrid (fiber-reinforced polymer-steel) reinforcements. J Compos Constr 2001; 6(2): 133-140.

[19] Yinghao L, Yong Y. Arrangements of hybrid rebars on flexural behavior of HSC beams. J Compos Part B 2013; 45:22-31.

[20] Qu W, Zhang X, Huang H. Flexural behavior of concrete beams reinforced with hybrid (GFRP and steel) bars. J Compos Constr 2009; 13(5):350-359.

[21] Mazaheripour H, Barros JAO, Sena-Cruz JM, Soltanzadeh F. Analytical bond model for GFRP bars to steel fiber reinforced self-compacting concrete. J Compos Constr 2013; 17(6).

[22] Soltanzadeh F, Mazaheripour H, Barros JAO, Taheri M, Sena-Cruz JM. Experimental study on shear behavior of HPFRC beams reinforced by hybrid pre-stressed GFRP and steel bars. In: Proceedings of the 7th International Conference on FRP composites in civil engineering (CICE 2014), Vancouver, Canada; Agust 2014. p. 20-22.

[23] Soltanzadeh F, Edalat-Behbahani A, Barros JAO, Mazaheripour H. Shear resistance of SFRSCC short-span beams without transversal reinforcements. J Compos Struct 2016; 139: 42-61.

[24] Soltanzadeh F, Mazaheripour H, Barros JAO, Sena-Cruz J. Shear capacity of HPFRC beams flexurally reinforced with steel and prestressed GFRP bars. In: Proceedings of the 11th International Conference on fiber reinforced polymers for reinforced concrete structure (FRPRCS-11), Guimaraes, Portugal, June 2013. p. 25-28.

[25] ACI Committee 544.1R-96. State-of-the-Art Report on Fiber Reinforced Concrete. ACI committee report; 1988. p. 66.

[26] EUROCODE 2. Design of concrete structures –Part 1-1: General rules and rules for buildings. UNI-ENV 1992-1-2; 2004.

[27] ACI Committee 318-11. Building code requirements for structural concrete and commentary. Farmington Hills (MI): American Concrete Institute; 2006. 44 pp.

[28] CEB-FIP Model Code 2010 - Final draft, 2011.

[29] RILEM TC162-TDF. Test and design methods for steel fiber reinforced concrete, $\sigma-\varepsilon$ design method. Final Recommendation. J Mater Struct 2003; 35:560-567.

[30] Soetens T. Design models for the shear strength of prestressed precast steel fiber reinforced concrete girders [Doctoral Thesis]. Belgium: Ghent University; 2015.

[31] Khuntia M, Stojadinovic B, Goel S. Shear strength of normal and high-strength fiber reinforced concrete beams without stirrups. ACI Struct J 1999; 96(2): 282-289.

[32] Ashour S, Hasanain G, Wafa F. Shear behavior of high-strength fiber reinforced concrete beams. ACI Struct J 1992; 89(2):176-184.

[33] Narayanan R, Darwish I. Use of steel fiber as shear reinforcement. ACI Struct J 1987; 84(3): 216-227.

[34] Soltanzadeh F, Barros JAO, Santos RFC. High performance fiber reinforced concrete for the shear reinforcement: Experimental and numerical research. J Constr Build Mater 2015; 77:94-109.

[35] BS EN 12350-8. Testing fresh concrete. Self-compacting concrete. Slump-flow test; 2010.

[36] Alberti MG, Enfedaque A, Galvez JC, Canovas MF, Osorio IR. Polyolefin fiber-reinforced concrete enhanced with steel-hooked fibers in low proportions. J Mater Des 2014; 60:57-65.

[37] Alberti MG, Enfedaque A, Galvez JC. On the mechanical properties and fracture behavior of polyolefin fiber-reinforced self-compacting concrete. J Constr Build Mater 2014; 55:274-288.

[38] BS EN 12390-13. Testing hardened concrete-Part 13: determination of secant modulus of elasticity in compression; 2014.

[39] ASTM C39/C39M-14a. Standard test method for compressive strength of cylindrical concrete specimens. Annual Book of ASTM Standard, Am Soc Test Mater 2014. doi: http://dx.doi.org/10.1520/c0039M-14A.

[40] Pereira EN, Barros JAO, Camoes A. Steel fiber-reinforced self-compacting concrete: experimental research and numerical simulation. J Struct Eng 2008; 134(8):1310-20.

[41] Chen B, Liu J. Effect of aggregate on the fracture behavior of high strength concrete. J Constr Build Mater 2004; 18(8):585-590.

[42] CAN/CSA-S06-06. The Canadian Highway Bridge design code (CHBDC), Canadian Standards Association, Ottawa, Ontario, Canada; 2006.

[43] ISIS Canada. A Canadian Network of Centres of Excellence. ISIS Educational Module 9: Prestressing

concrete structures with fibre reinforced polymers 2007; 10:2(139).

[44] EN 1992-1-1. Design of concrete structures. Part 1-1: general rules and rules for buildings; 2004.

[45] ASTM D7205/D7205M-06. Standard test method for tensile properties of fiber reinforced polymer matrix composite bars. Annual Book of ASTM Standard, Am Soc Test Mater 2006.

[46] Mazaheripour H. Structural behavior of hybrid GFRP and steel reinforced FRC prestressed beams [Doctoral thesis]. Portugal: University of Minho; 2016.

[47] Grace NF, Singh SB. Design approach for carbon fiber-reinforced polymer prestressed concrete bridge beams. ACI Mater J 2003; 100(3): 365-376.

[48] Bischoff PH. Deflection calculation of FRP reinforced concrete beams based on modifications to the existing Branson equation. J Compos Constr 2007; 11(1): 4-14.

[49] Leung HY, Balendran RV. Flexural behaviour of concrete beams internally reinforced with GFRP reds and steel rebars. J Struct Survey 2003; 21(4): 146-157.

[50] El-mihilmy M, Tedesco J. Analysis of reinforced concrete beams strengthened with FRP laminates. J Struct Eng 2000; 126(6): 684-691.

[51] ACI Committee 440.2R-08. Guide for the design and construction of externally bonded FRP systems for strengthening concrete structures. ACI committee report; 2008. p. 78.

[52] ASCE-ACI Committee 426. The shear strength of reinforced concrete members. J Struct Div 1973; 99(6): 1091-1187.

[53] ACI440.IR-06. Guide for the design and construction of structural concrete reinforced with FRP bars. ACI committee report; 2006. p. 44.

[54] Mazaheripour H, Barros JAO, Sena-Cruz JM. Tension-stiffening model for FRC reinforced by hybrid FRP and steel bars. J Compos Part B 2016; 88:162-181.

[55] Sena-Cruz JM, Barros JAO, Azevedo AFM, Ventura-Gouveia A. Numerical simulation of the nonlinear behaviour of RC beams strengthened with NSM CFRP strips. In: Proceedings of CMNE/CILAMCE, Porto, Portugal; June 2007.

[56] Edalat-Behbahani A, Barros JAO, Ventura-Gouveia A. Plastic-damage smeared crack model to simulate the behaviour of structures made by cement based materials. J Solid Struct 2015; 73-74: 20-40.

[57] Ventura-Gouveia A. Constitutive models for the material nonlinear analysis of concrete structures including time dependent effects [Doctoral thesis]. Portugal: University of Minho; 2011.

[58] Sena-Cruz JM. Strengthening of concrete structures with near-surface mounted CFRP laminate strips [Doctoral thesis]. Portugal: University of Minho; 2004.

[59] Cunha VMCF, Barros JAO, Sena-Cruz JM. Afinite element model with discrete embedded elements for fiber reinforced composites. J Comp Struct; 2012; 94-95:22-33.

[60] Minelli F, Conforti A, Cuenca E, Plizzari G. Are steel fibers able to mitigate or eliminate size effect in shear? J Mater Struct 2013; 47: 459-473.

Notation

A_{GFRP}	cross section area of GFRP rebar
A_s	cross section area of steel bar
A_{sw}	cross section area of a steel stirrup
a	shear span of beam
b_f	flange width
b_w	web width
c_b	depth of neutral axis
d	effective depth of beam
d_c	scalar compressive damage variable
d_{GFRP}	GFRP internal arm
d_s	steel internal arm
$d_{s,eq}$	equivalent internal arm
E_{GFRP}	modulus of elasticity of GFRP bar
E_{cm}	compressive modulus of elasticity of concrete
E_s	modulus of elasticity of steel strand.
e	distance between the top of FRC tensile block to the top fiber of the beam cross section

F_{SLS}	load carrying capacity at SLS
$F_{\max}$	maximum load carrying capacity
$F_{\max}^{Num}$	maximum load carrying capacity obtained by FEM based numerical model
f_{Ftuk}	Characteristic value of ultimate residual tensile strength of FRC
f_{Ftum}	average value of ultimate residual tensile strength of FRC
f_{Rj}	residual flexural tensile strength, corresponding $CMOD_j$ (j=1, 2,3,4)
f_{ck}	characteristic value of concrete compressive strength
f_{cm}	mean value of concrete compressive strength
f_{ctm}	mean value of concrete tensile strength
f_{su}	ultimate tensile strength of steel bar
f_{sy}	nominal yield strength of steel strand
f_{ywd}	design value of yield stress of shear reinforcement
$f_{ct,L}^{f}$	stress at limit of proportionality,
f_{c0}	uniaxial compressive stress at plastic threshold
$G_{f,c}$	compressive fracture energy
$G_{f,s}$	mode II fracture energy
G_f^{I}	mode I fracture energy
h	height of beam
IP	integration point
k	size effect factor
k_f	factor for taking into account the contribution of the flange in T-sections
L	span of beam
l_c	characteristic length in compression
P	applied load
s	spacing of stirrups

V_{MC2010}	estimated shear resistance according to MC2010 approach
V_{RILEM}	estimated shear resistance according to RILEM TC 162-TDF approach
$V_{Soetens2010}$	estimated shear resistance according to Soetens (2015) formula
V_{cd}	design value of shear resistance attributed to plain concrete
$V_{\exp}$	shear resistance of beams obtained experimentally
V_f	fiber volume fraction
V_{fd}	design value of shear resistance attributed to steel fibers
V_{nz}	normalized shear resistance
V_{wd}	design value of shear resistance attributed to transversal reinforcement
v_u	ultimate shear strength
z	internal lever arm of beam
α_0	material constant to define the beginning of the nonlinear behavior in uniaxial compressive stress-strain test
β_1	ratio of the equivalent rectangular stress block depth to the depth of neutral axis
β_2	a parameter for accounting the particular geometry of I-shape cross section
γ_c	partial safety factor for the material properties
γ_t^{cr}	shear component of the crack strain vector
$\gamma_{t,p}^{cr}$	peak crack shear strain
δ	deflection at mid-span of beam
$\varepsilon_{STIRRUP}$	strain in steel stirrup
ε_{GFRP}	strain in GFRP rebar
$\varepsilon_{GFRP,u}$	ultimate strain of GFRP rebar
ε_{STRAND}	strain in steel strand
ε_{cu}	ultimate compressive strain of concrete
ε_n^{cr}	normal component of the crack strain vector

ε_{GFRP}^{pre}	strain in GFRP rebar due to application of prestress
$\tilde{\epsilon}_c$	compressive hardening variable
$\tilde{\epsilon}_{cu}$	maximum equivalent strain in compression
$\tilde{\epsilon}_{c1}$	hardening parameter at compressive strength
ξ_i	normalized strain parameter (i=1,2,3) in quadrilinear diagram
ρ_{GFRP}	reinforcement ratio of longitudinal GFRP rebars
ρ_{fb}	balanced reinforcement ratio
ρ_s	reinforcement ratio of longitudinal steel reinforcements
$\rho_{s,eq}$	equivalent steel reinforcement ratio
ρ_{sw}	shear reinforcement ratio
σ_f	nominal flexural stress
σ_{cp}	average stress acting on the concrete cross section
σ_n^{cr}	normal components of the crack stress vector
$\bar{\sigma}_c$	hardening function of the plasticity model
τ_t^{cr}	shear component of the crack stress vector
$\tau_{t,p}^{cr}$	crack shear strength

Figure captions

Fig. 1 -	Nominal flexural stress, σ_f , *vs.* CMOD relationship.
Fig. 2 -	Geometry, reinforcement and test setup of the beams of the (a) group 1 and (b) group 2 (dimensions in mm).
Fig. 3 -	(a) Strain and stress distribution at ultimate state conditions of I-shaped cross section beam and (b) cross section area under F_{st} and F_{GFRP} forces.
Fig. 4 -	(a) Load, *P*, *vs.* mid-span deflection relationship and (b) crack pattern at failure of the first and second group of beams.
Fig. 5 -	Load *vs.* strain in GFRP bars at mid-span of (a) the first and (b) second group of beams.
Fig. 6 -	Load *vs.* strain in steel stirrups at shear span of the beam G2-F0-ST.
Fig. 7 -	Constitutive models for the constituent materials: (a) concrete fracture mode I; (b) concrete fracture mode II; (c) hardening function-hardening parameter law; (d) evolution of the scalar damage variable as function of the hardening parameter; (e) stress-strain diagram for steel reinforcement.
Fig. 8 -	Finite element mesh, load and support conditions used for analysis of the beam G1-F1.1-S0.
Fig. 9 -	Experimental and numerical load *vs.* mid-span deflection of the beams of the first group: (a) G1- F1.1-S0; (b) G1- F1.1-S23; (c) G1- F1.1-S46.
Fig. 10 -	Experimental and numerical load *vs.* mid-span deflection of the beams of the second group: (a) G2- F0; (b) G2- F0-ST; (c) G2- F1.1; (d) G2-F1.5.
Fig. 11 -	Numerical crack pattern predicted by PDSC model for the beam G2- F1.5 (The results correspond to the final converged step). Note: In pink color: crack completely open; in red color: crack in the opening process; in cyan color: crack in the reopening process; in green color: crack in the closing process; in blue color: closed crack; in red circle: the plastic zone.
Fig. 12 -	Experimental and numerical load versus the strain in steel stirrups of beam G2-F0-ST.
Fig. 13 -	Experimental and numerical load versus GFRP strain at mid-span of the beams.
Fig. 14 -	Numerical load versus the strain of strand in mid-span of the beams relationships.
Fig. 15 -	Contribution of concrete and shear reinforcement (i.e. steel fibers and stirrups) to the shear capacity of the beams.

Table captions

Table-1	Concrete compositions executed with different dosages steel fiber.
Table-2	2 Limit of proportionality and residual flexural strength parameters of the developed concrete mixes.
Table-3	Details of the developed beams in first and second group.
Table-4	Summary of the test results.
Table-5	Values of the parameters of the steel constitutive model.
Table-6	General information about the simulation of the prestress load by means of temperature variation.
Table-7	Values of the parameters of the constitutive model for concretes SCC-F0, SCC-F1.1, and SCC-F1.5.
Table-8	Details of the experimental results and the numerical analysis.
Table-9	MC2010 [28] and RILEM TC 162-TDF [29] and Soetens [30] approaches for predicting shear resistance of FRC beams.
Table-9	Shear resistance calculated analytically in comparison with the experimental results.

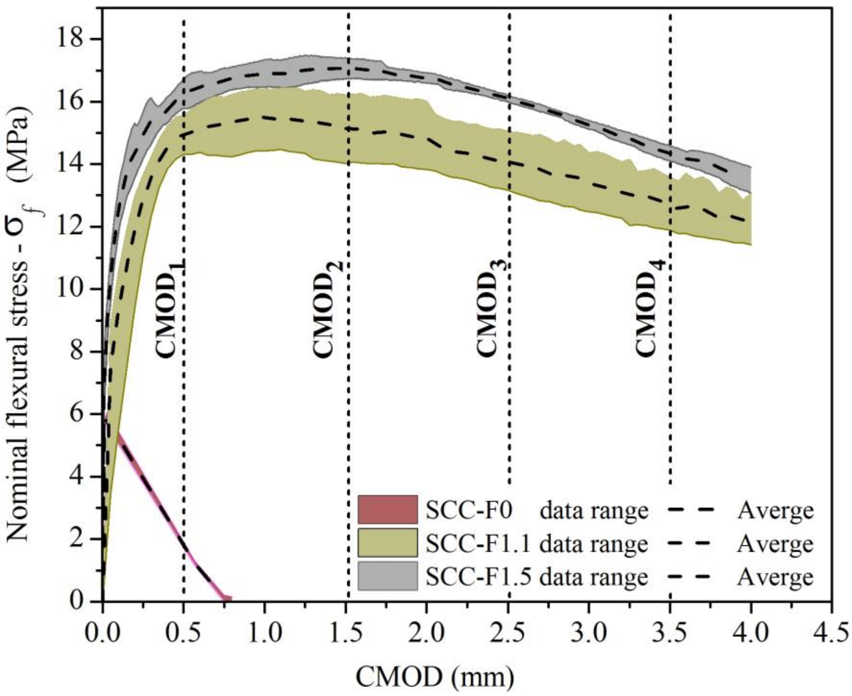

Fig. 1 - Nominal flexural stress, σ_f , *vs.* CMOD relationship.

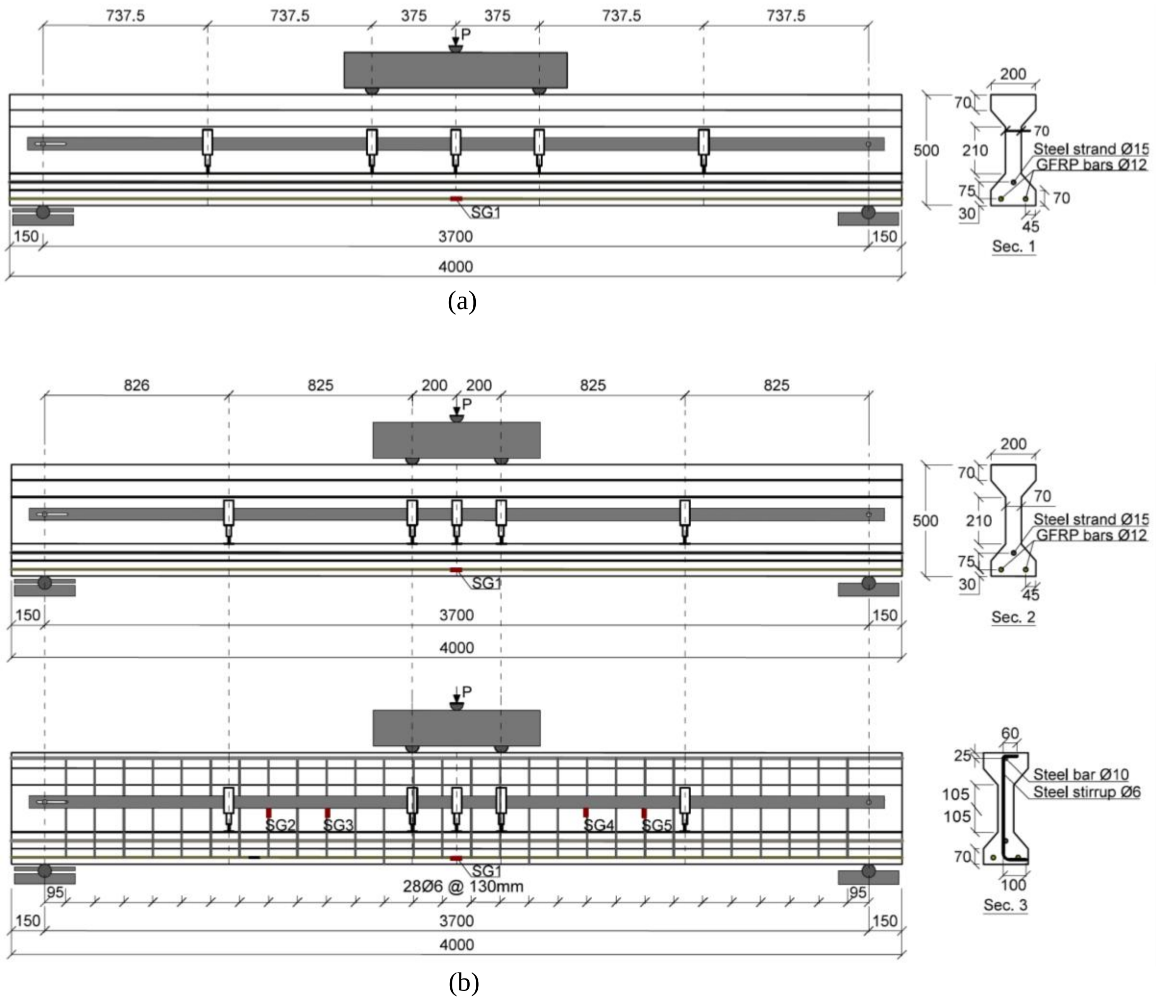

Fig. 2 - Geometry, reinforcement and test setup of the beams of the (a) group 1 and (b) group 2 (dimensions in mm).

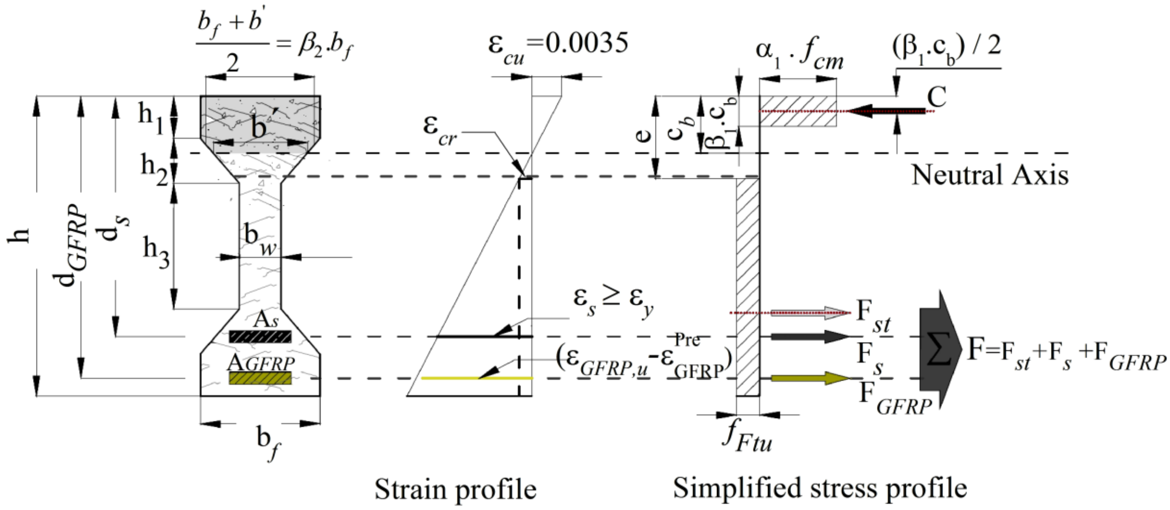

(a)

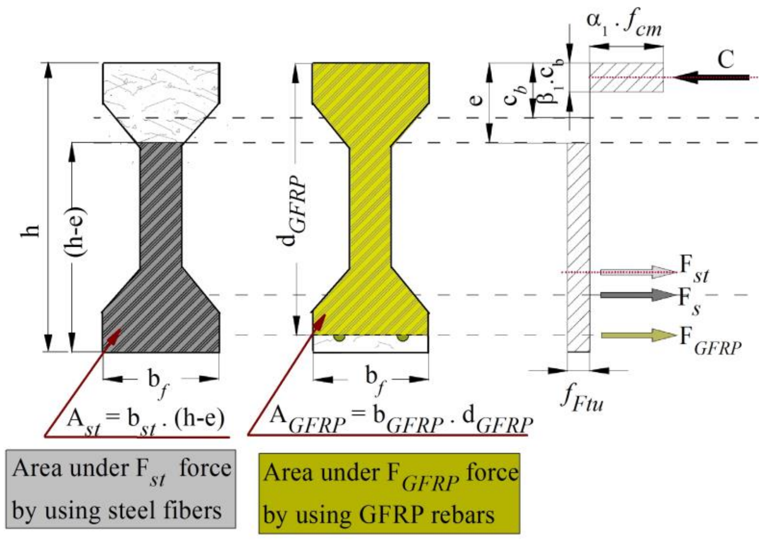

(b)

C : concrete compressive force,

F_{st} : steel fiber tensile force,

F_s :tensile force in steel reinforcement,

F_{GFRP} : tensile force in GFRP bars,

ε_{cr} : strain at crack initiation.

$\alpha = \beta_1 . c_b$: depth of the compressive block.

Fig. 3 – (a) Strain and stress distribution at ultimate state conditions of I-shaped cross section beam and (b) cross section area under F_{st} and F_{GFRP} forces.

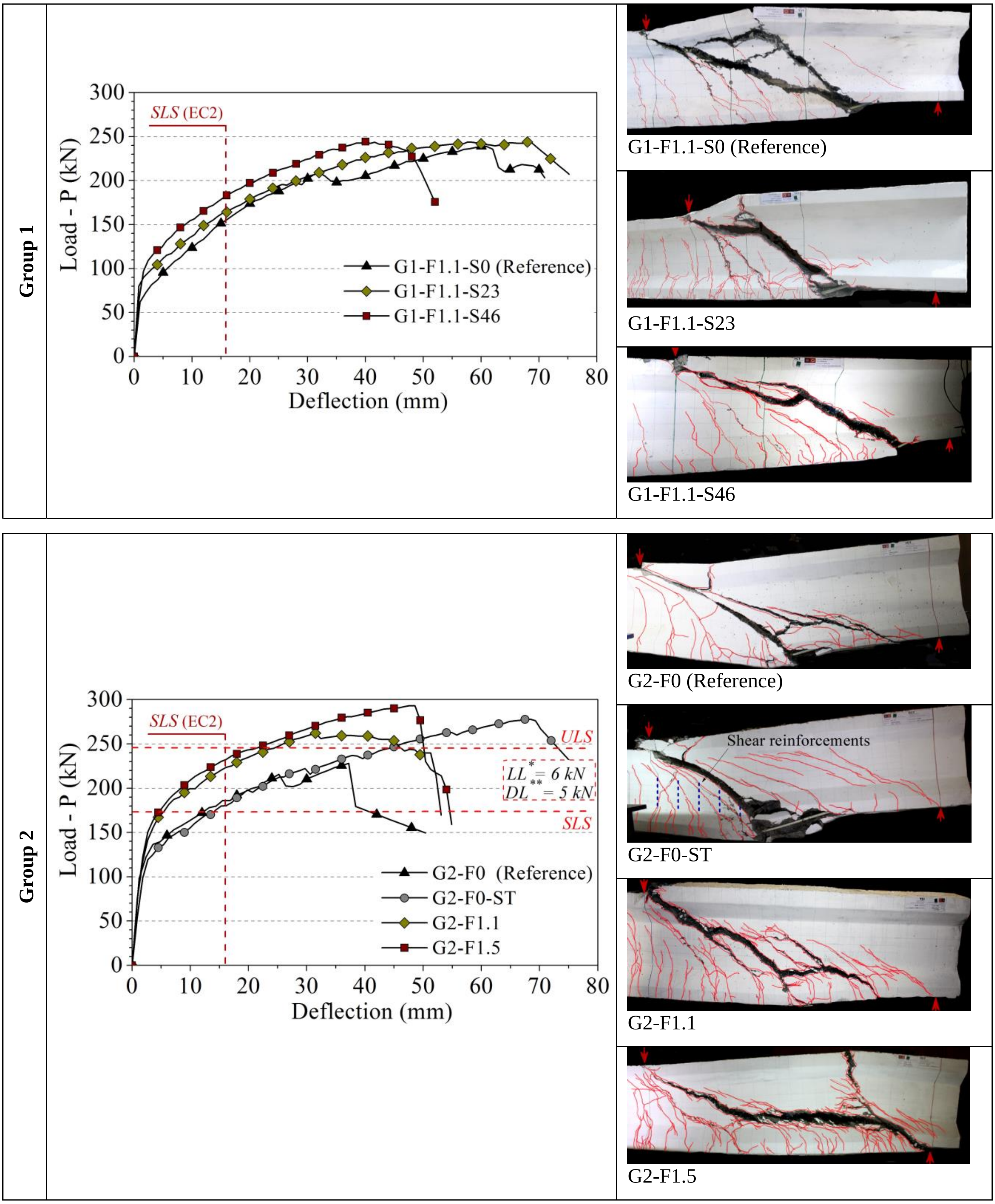
Group 1
Load - P (kN)
Deflection (mm)
SLS (EC2)
G1-F1.1-S0 (Reference)
G1-F1.1-S23
G1-F1.1-S46
G1-F1.1-S0 (Reference)
G1-F1.1-S23
G1-F1.1-S46
Group 2
Load - P (kN)
Deflection (mm)
SLS (EC2)
ULS
SLS
LL* = 6 kN
DL** = 5 kN
G2-F0 (Reference)
G2-F0-ST
G2-F1.1
G2-F1.5
G2-F0 (Reference)
Shear reinforcements
G2-F0-ST
G2-F1.1
G2-F1.5

(a) (b)

Fig. 4 – (a) Load, *P*, *vs.* mid-span deflection relationship and (b) crack pattern at failure of the first and second group of beams.

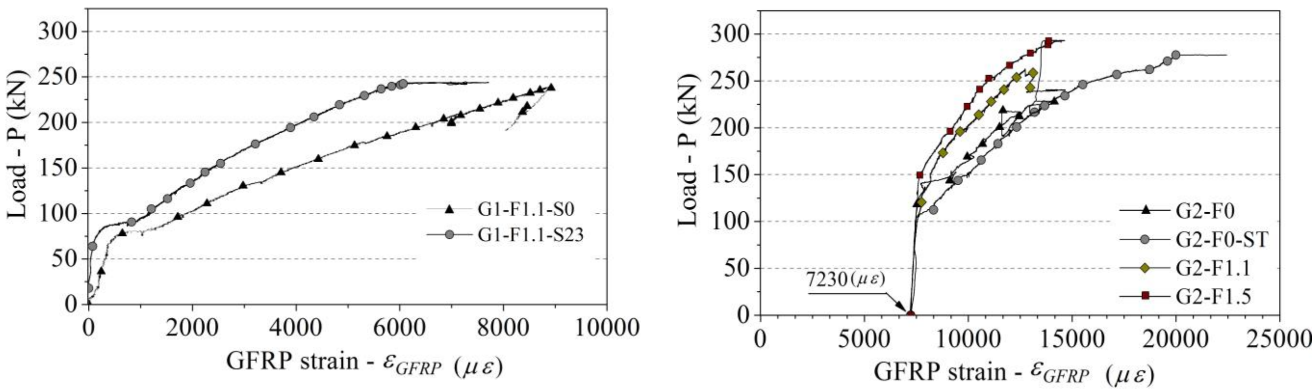

(a) (b)

Fig. 5 - Load *vs.* strain in GFRP bars at mid-span of (a) the first and (b) second group of beams.

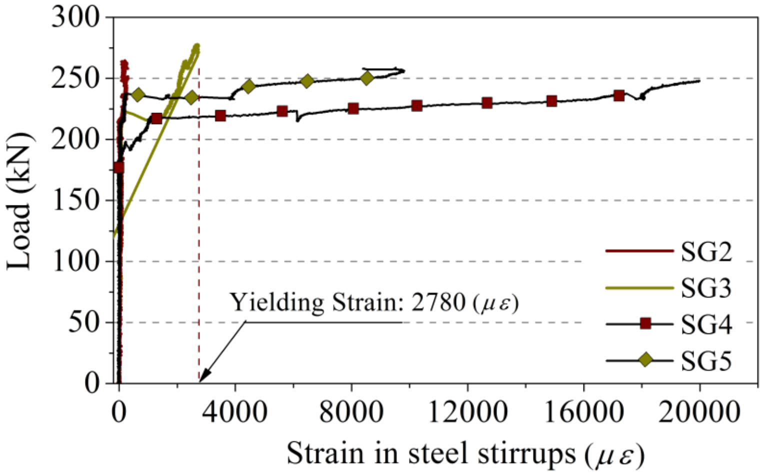

Fig. 6 - Load *vs.* strain in steel stirrups at shear span of the beam G2-F0-ST.

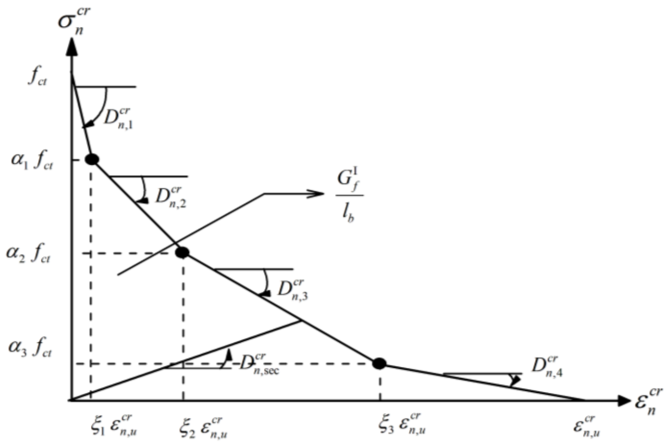

(a)

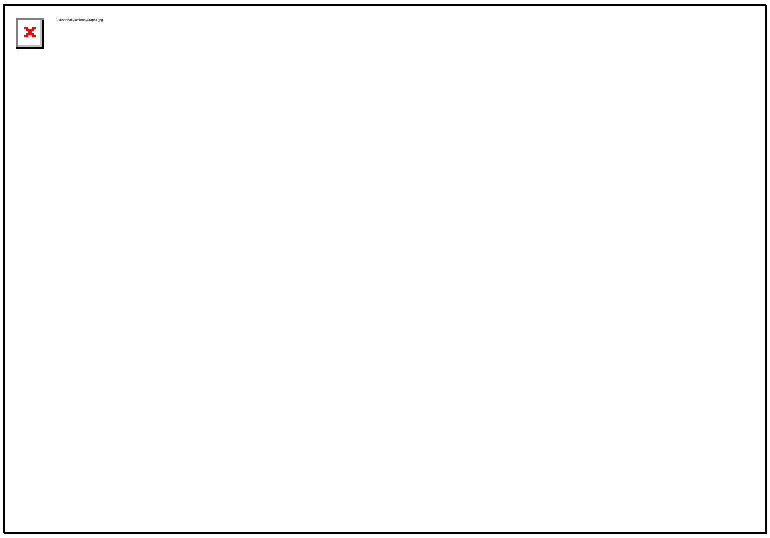

(b)

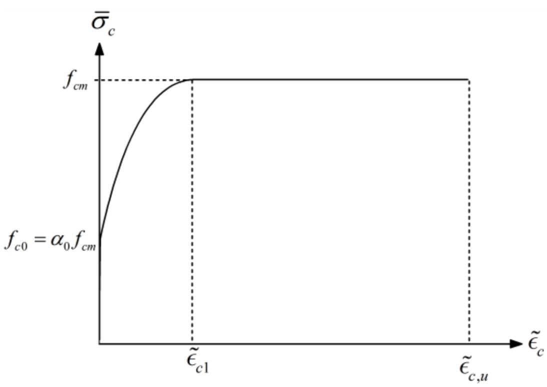

(c)

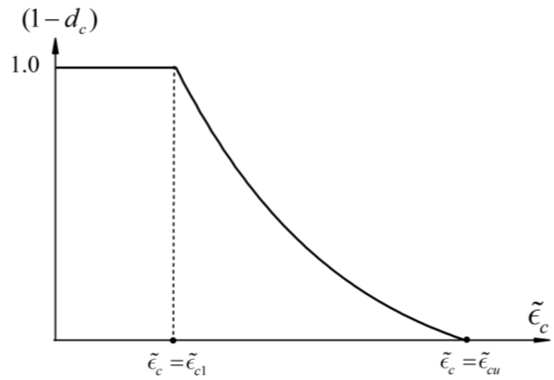

(d)

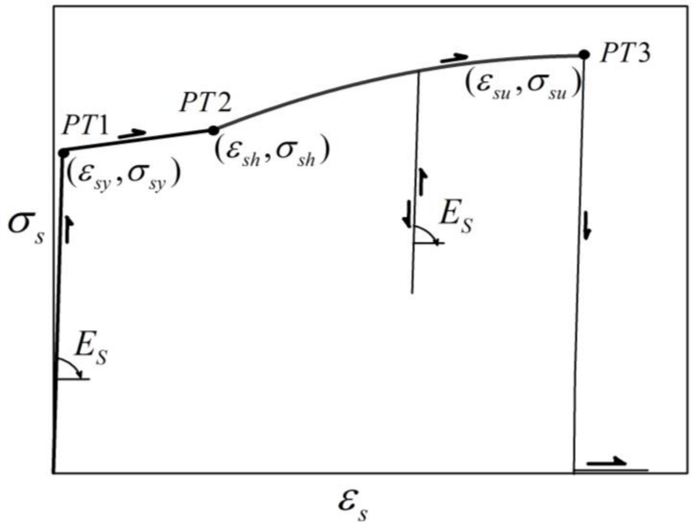

(e)

Fig. 7 - Constitutive models for the constituent materials: (a) concrete fracture mode I; (b) concrete fracture mode II; (c) hardening function-hardening parameter law; (d) evolution of the scalar damage variable as function of the hardening parameter; (e) stress-strain diagram for steel reinforcement.

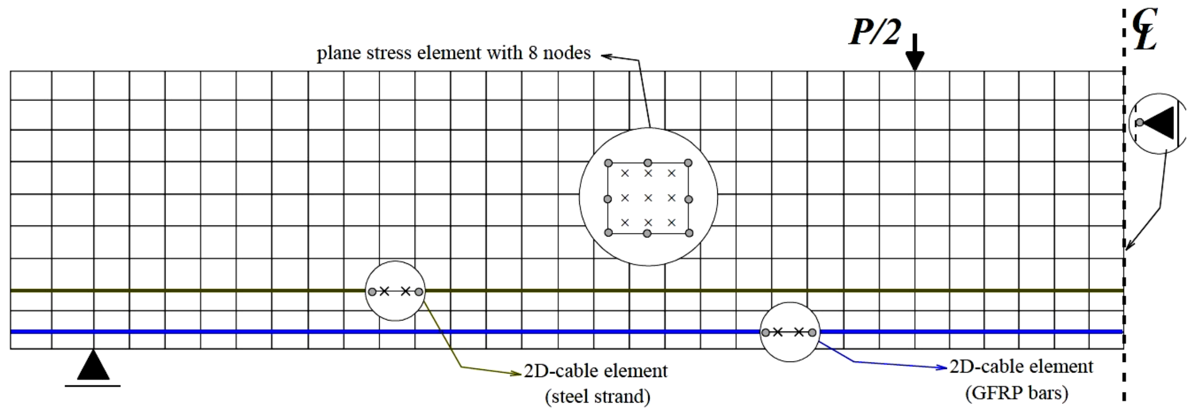

Fig. 8 - Finite element mesh, load and support conditions used for analysis of the beam G1-F1.1-S0.

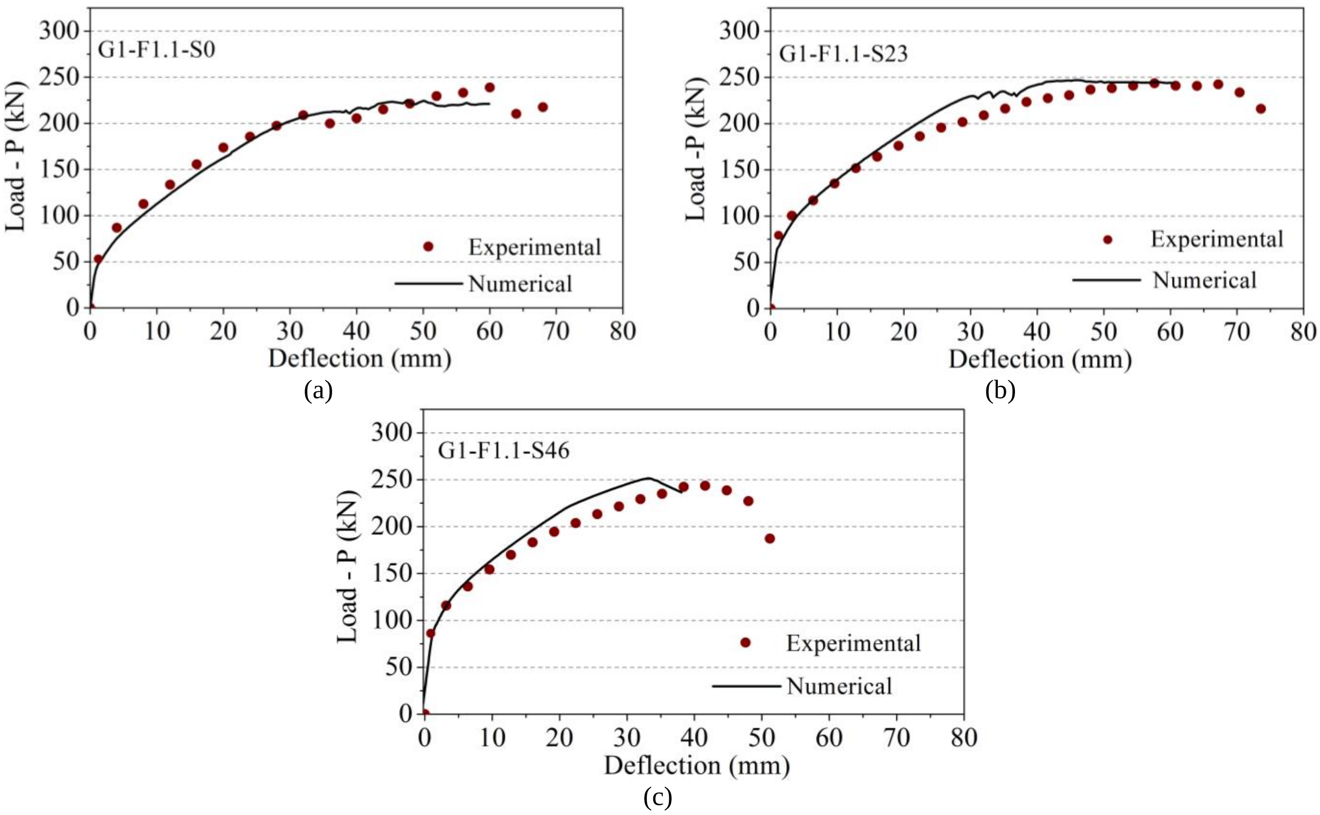

Fig. 9 - Experimental and numerical load *vs.* mid-span deflection of the beams of the first group: (a) G1- F1.1-S0; (b) G1-F1.1-S23; (c) G1- F1.1-S46.

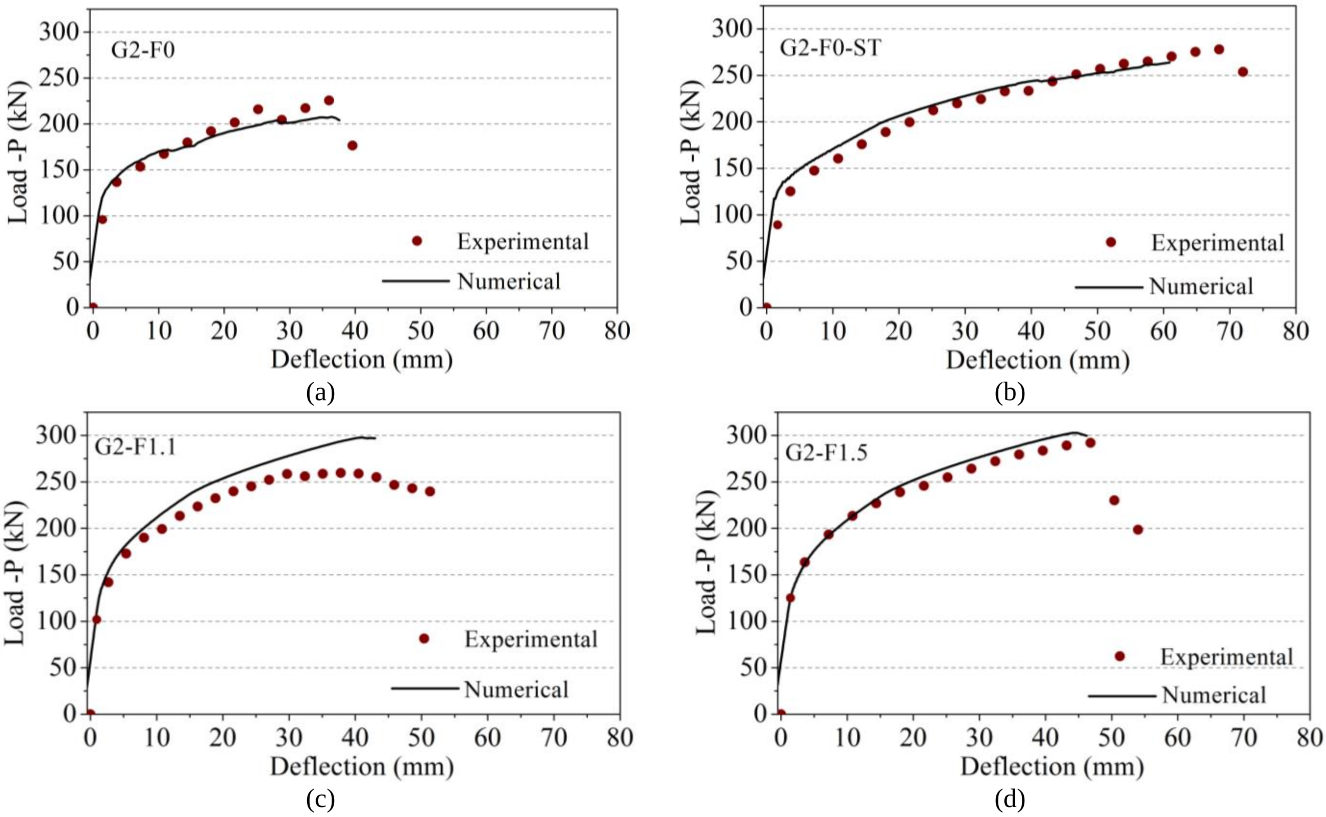

Fig. 10 - Experimental and numerical load *vs.* mid-span deflection of the beams of the second group: (a) G2- F0; (b) G2- F0-ST; (c) G2- F1.1; (d) G2-F1.5.

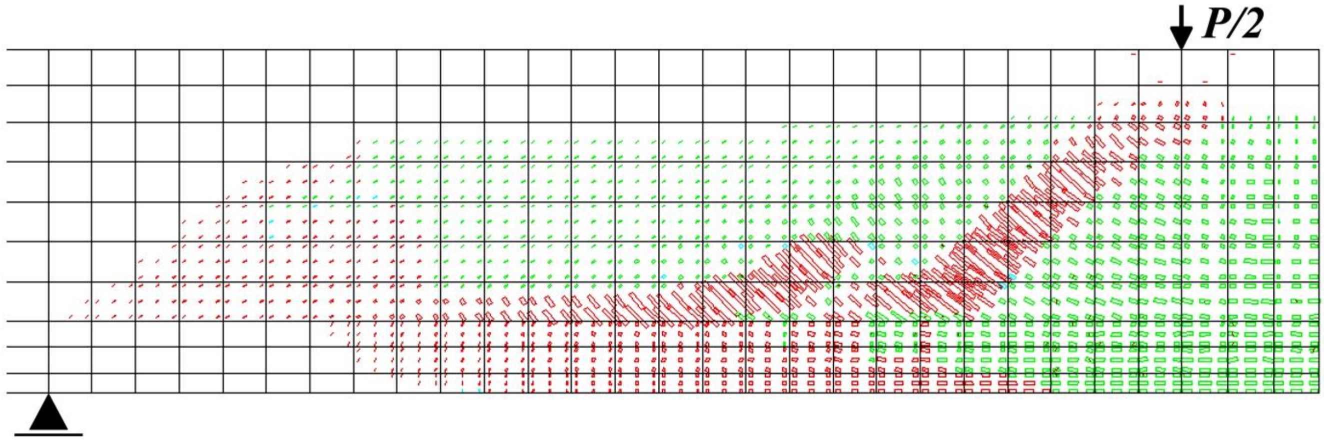

Fig. 11 - Numerical crack pattern predicted by PDSC model for the beam G2- F1.5 (The results correspond to the final converged step).

Note: In pink color: crack completely open; in red color: crack in the opening process; in cyan color: crack in the reopening process; in green color: crack in the closing process; in blue color: closed crack; in red circle: the plastic zone.

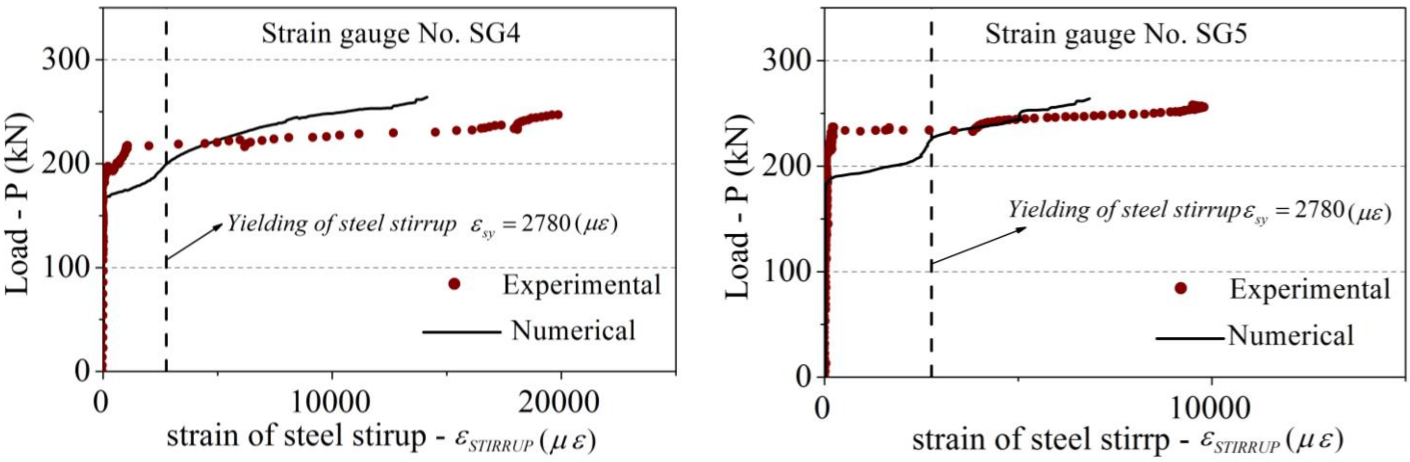

(a) (b)

Fig. 12 - Experimental and numerical load versus the strain in steel stirrups of beam G2-F0-ST.

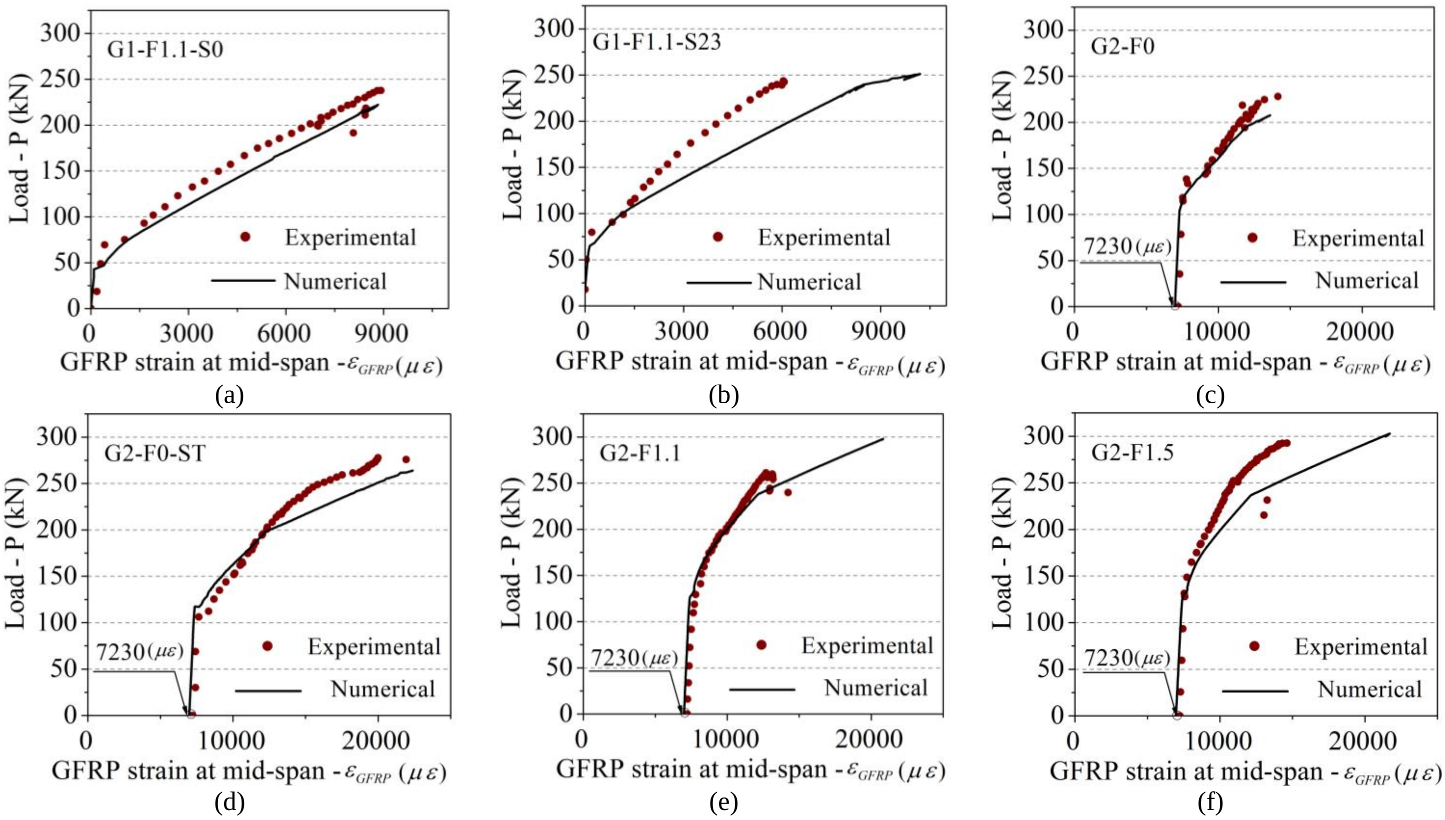

Fig. 13 - Experimental and numerical load versus GFRP strain at mid-span of the beams.

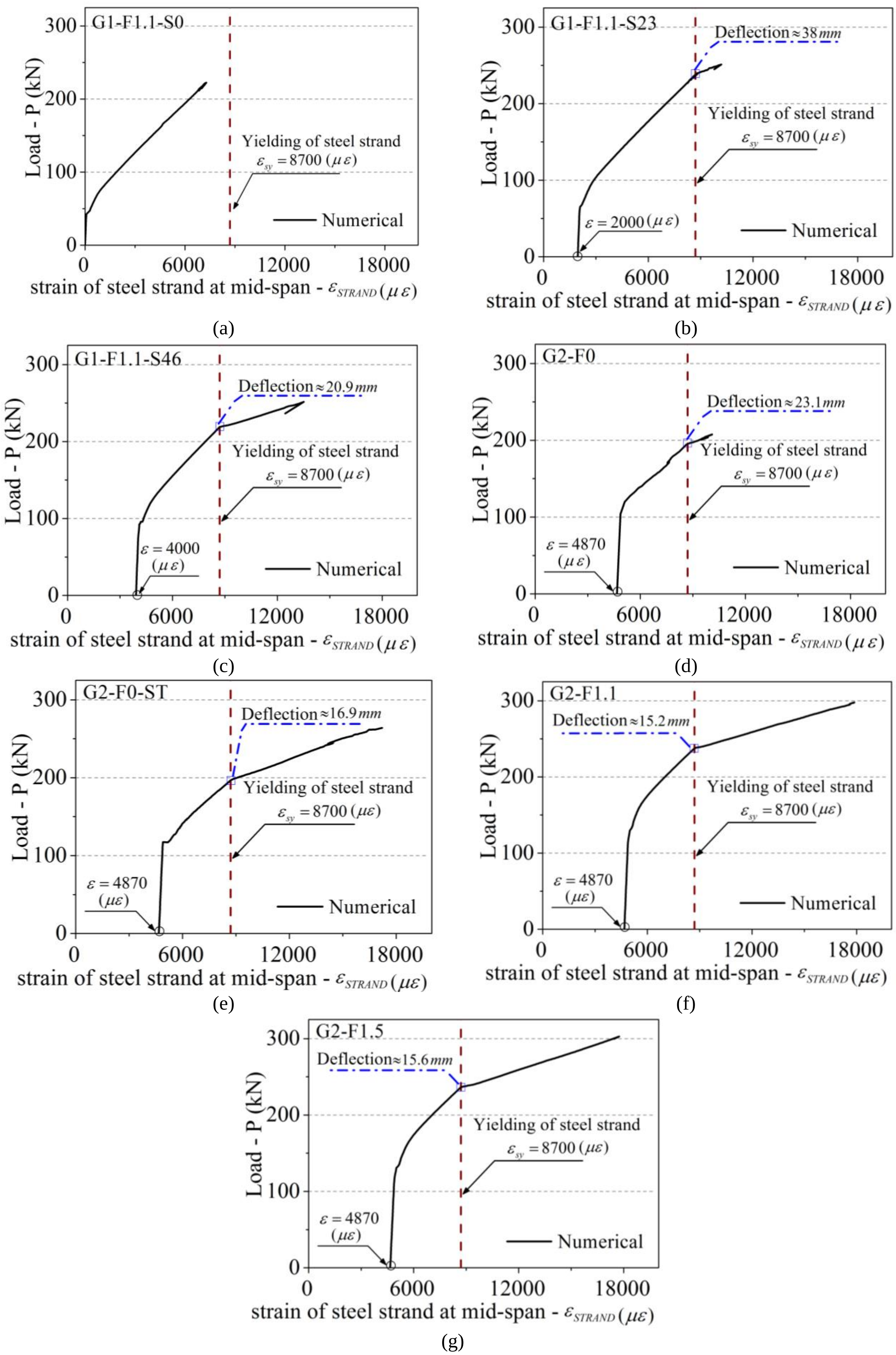

Fig. 14 - Numerical load versus the strain of strand in mid-span of the beams relationships.

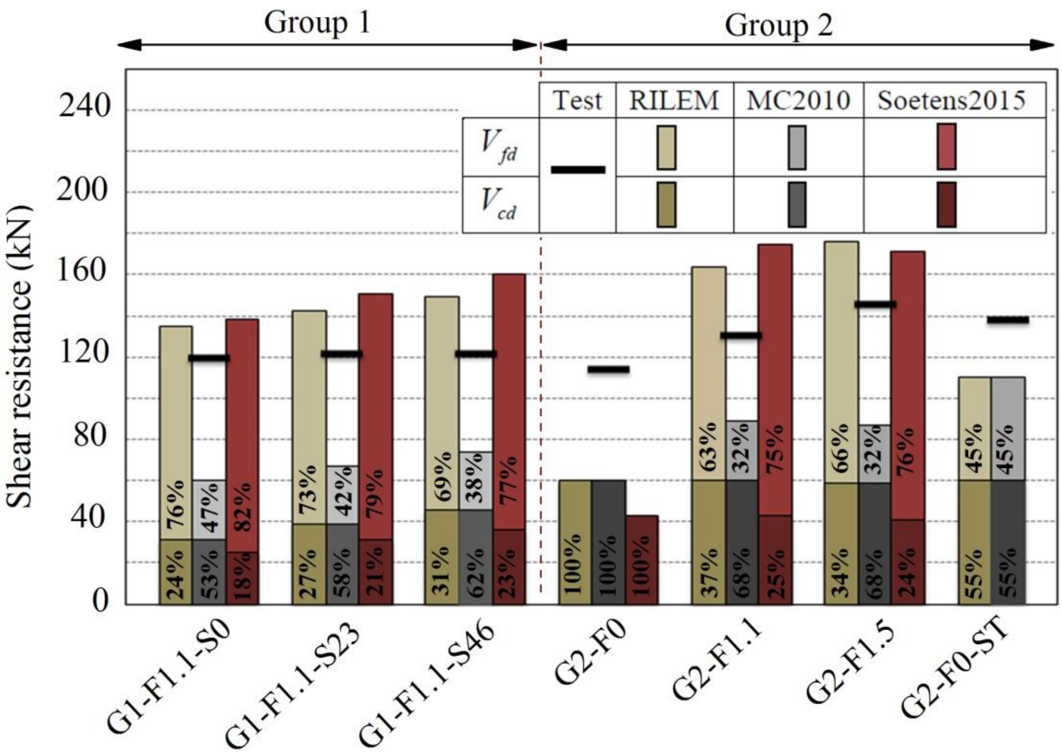

Fig. 15 - Contribution of concrete and shear reinforcement (i.e. steel fibers and stirrups) to the shear capacity of the beams.

Table-1 Concrete compositions executed with different dosages steel fiber.

Mix ID	C[a] (kg/m^3)	FA[b] (kg/m^3)	LF[c] (kg/m^3)	W[d] (L/m^3)	SP[e] (L/m^3)	FS[f] (kg/m^3)	CS[g] (kg/m^3)	CA[h] (kg/m^3)	SF[i] (kg/m^3)	PF[j] (kg/m^3)
SCC-F0	462	140	140	197	15.7	126	670	512	0	3
SCC-F1.1	472	141	142	201	16.0	123	656	503	90	3
SCC-F1.5	551	165	165	235	18.7	125	521	425	120	3

[a] Cement, [b] Fly Ash, [c] Limestone Filler, [d] Mixing Water, [e] Superplasticizer, [f] Fine Sand, [g] Coarse Sand, [h] Coarse Agg., [i] Steel Fibers, [j] Synthetic (Polyolefin Based) Macro Fibers.

Table-2 Limit of proportionality and residual flexural strength parameters of the developed concrete mixes.

Mix ID		$f^{f}_{ct,L}$ (MPa)	f_{R1} (MPa)	f_{R2} (MPa)	f_{R3} (MPa)	f_{R4} (MPa)	$f_{R3k}{}^{a}$ / $f_{R1k}{}^{b}$
			$CMOD_1$= 0.5 mm	$CMOD_2$= 1.5 mm	CMOD3= 2.5 mm	$CMOD_4$= 3.5 mm	
SCC-F0	Average	5.72	1.2	-	-	-	-
	CoV (%)	4.4	7.7	-	-	-	-
SCC-F1.1	Average	7.6	14.95	15.14	14.08	12.67	1.05
	CoV (%)	18.6	6.3	7.5	0.9	13.1	-
SCC-F1.5	Average	10.32	16.23	17.06	16.1	14.33	1.06
	CoV (%)	10.52	4.1	2.7	1.0	2.3	-

[a] Characteristic tensile flexural strength at CMOD=2.5mm.

[b] Characteristic tensile flexural strength at CMOD=0.5mm.

Table-3 Details of the developed beams in first and second group.

Specimen ID		Concrete type	Prestress level of the beams in the testing day		V_f (%)	$d_{s,eq}$ (mm)
			Strand (% of f_{sy}; stress level in MPa)	GFRP (% of $f_{GFRP,u}$; stress level in MPa)		
Group 1	G1-F1.1-S0	SCC-F1.1	0; 0	0	1.1	418
	G1-F1.1-S23	SCC-F1.1	23; 400	0	1.1	418
	G1-F1.1-S46	SCC-F1.1	46; 800	0	1.1	418
Group 2	G2-F0	SCC-F0	56;974	30;405	0	418
	G2-F0-ST	SCC-F0	56;974	30;405	0	418
	G2-F1.1	SCC-F1.1	56;974	30;405	1.1	418
	G2-F1.5	SCC-F1.5	56;974	30;405	1.5	418

Table-4 Summary of the test results.

	Specimen ID	F_{SLS} [a] (KN)	Increase of F_{SLS} [b] (%)	$F_{\max}$ [c] (KN)	Increase of $F_{\max}$ [d] (%)	$\delta_{\max}$ [e] (mm)	V_{nz} (MPa)$^{0.5}$
Group 1	G1-F1.1-S0 (Reference)	151.42	-	240.12	-	60.71	0.501
	G1-F1.1-S23	161.98	7.0	244.80	1.9	67.68	0.511
	G1-F1.1-S46	178.14	17.6	245.60	2.3	40.21	0.513
Group 2	G2-F0 (Reference)	187.83	-	229.52	-	37.14	0.481
	G2-F0-ST	179.27	-	277.98	21.0	68.35	0.583
	G2-F1.1	222.93	18.7	263.00	14.6	32.70	0.550
	G2-F1.5	229.84	22.4	293.75	27.9	47.39	0.601

[a] F_{SLS} Load at serviceability limit state by deflection (16 mm).

[b] Increase of F_{SLS} when compared to that of the corresponding reference beam.

[c] $F_{\max}$ Maximum load.

[d] Increase of $F_{\max}$ when compared to that of the corresponding reference beam.

[e] $\delta_{\max}$ Deflection corresponding to $F_{\max}$.

Table-5 Values of the parameters of the steel constitutive model.

Diameter (mm)	ε_{sy}(%)	$\sigma_{sy}\,(N/mm^2)$	ε_{sh}(%)	$\sigma_{sh}\,(N/mm^2)$	ε_{su}(%)	$\sigma_{su}\,(N/mm^2)$	Third branch exponent
[a] 15.2	0.87	1740	0.87	1740	20.0	1917	1
[b] 10	0.28	566	1	594	10.0	661	1
[c] 6	0.278	556	1	583	10.0	682	1

[a] steel strand; [b] compressive reinforcement; [c] stirrups.

Table-6 General information about the simulation of the prestress load by means of temperature variation.

Specimen ID	[a] $\sigma_{t,S}$ (MPa)	[b] $\sigma_{t,GFRP}$ (MPa)	[c] $\alpha (mm/(mm\,^{o}C))$	[d] $\Delta T_S\,(^{o}C)$	[e] $\Delta T_{GFRP}\,(^{o}C)$
G1-F1.1-S0	-	-	-	-	-
G1-F1.1-S23	400	-	1×10^{-5}	-200	-
G1-F1.1-S46	800	-	1×10^{-5}	-400	-
G2-F0	974	405	1×10^{-5}	-487	-723
G2-F0-ST	974	405	1×10^{-5}	-487	-723
G2-F1.1	974	405	1×10^{-5}	-487	-723
G2-F1.5	974	405	1×10^{-5}	-487	-723

[a] $\sigma_{t,S}$ thermal stress applied to the steel strand; [b] $\sigma_{t,GFRP}$ thermal stress applied to the GFRP bars; [c] α coefficient of thermal expansion; [d] $\Delta T_S\,(^{o}C)$ temperature variation applied to the steel strand; [e] $\Delta T_{GFRP}\,(^{o}C)$ temperature variation applied to the GFRP bars.

Note: the thermal strain and corresponding stress for the steel strand are calculated from: $\varepsilon_{t,S} = \alpha\,\Delta T_S$; $\sigma_{t,S} = E_S\,\varepsilon_{t,S}$. For the GFRP bars the following equations are taken: $\varepsilon_{t,\mathrm{GFRP}} = \alpha\,\Delta T_{GFRP}$; $\sigma_{t,\,GFRP} = E_{GFRP}\,\varepsilon_{t,\mathrm{GFRP}}$.

Table-7 Values of the parameters of the constitutive model for concretes SCC-F0, SCC-F1.1, and SCC-F1.5.

Property	Value
Poisson's coefficient	$\nu = 0.2$
Young's modulus	for SCC-F0 $E_{cm} = 32100\, N/mm^2$; for SCC-F1.1 $E_{cm} = 33230\, N/mm^2$; for SCC-F1.5 $E_{cm} = 30580\, N/mm^2$
Parameters defining the plastic-damage part of the model (Fig. 7(c) and (d))	for SCC-F0 $f_c = 66.45\, N/mm^2; G_{f,c} = 25.0\, N/mm;\ \varepsilon_{c1} = 0.0035; \alpha_0 = 0.4$; for SCC-F1.1 $f_c = 67.05\, N/mm^2; G_{f,c} = 55.0\, N/mm;\ \varepsilon_{c1} = 0.004; \alpha_0 = 0.4$; for SCC-F1.5 $f_c = 60.03\, N/mm^2; G_{f,c} = 65.0\, N/mm;\ \varepsilon_{c1} = 0.004; \alpha_0 = 0.4$
Parameter defining the quadrilinear tension-softening diagram (Fig. 7(a))	for SCC-F0: $f_{ct} = 3.25\, N/mm^2; G_f^{\mathrm{I}} = 0.08\, N/mm;$ $\xi_1 = 0.007; \alpha_1 = 0.3; \xi_2 = 0.1; \alpha_2 = 0.15; \xi_3 = 0.15; \alpha_3 = 0.05$; for SCC-F1.1: $f_{ct} = 3.25\, N/mm^2; G_f^{\mathrm{I}} = 6.0\, N/mm;$ $\xi_1 = 0.0005; \alpha_1 = 0.75; \xi_2 = 0.0025; \alpha_2 = 1.0; \xi_3 = 0.1; \alpha_3 = 0.6$; for SCC-F1.5: $f_{ct} = 3.25\, N/mm^2; G_f^{\mathrm{I}} = 7.5\, N/mm;$ $\xi_1 = 0.0005; \alpha_1 = 0.75; \xi_2 = 0.0025; \alpha_2 = 1.0; \xi_3 = 0.1; \alpha_3 = 0.6$
Parameter defining the mode I fracture energy available to a new crack (Sena-Cruz [58])	2
Parameters defining the crack shear stress-crack shear strain diagram (Fig. 7(b))	for SCC-F0: $\tau_{t,p}^{cr} = 1.2\ N/mm^2; \beta = 0.4; G_{f,s} = 0.08\ N/mm$; for SCC-F1.1: $\tau_{t,p}^{cr} = 1.75\ N/mm^2; \beta = 0.2; G_{f,s} = 1.5\ N/mm$; for SCC-F1.5: $\tau_{t,p}^{cr} = 1.75\ N/mm^2; \beta = 0.2; G_{f,s} = 2.0\ N/mm$
Crack bandwidth	square root of the area of Gauss integration point
Threshold angle (Sena-Cruz [58])	30 degrees
Maximum number of cracks per integration point (Sena-Cruz [58])	2

Table- 8 Details of the experimental results and the numerical analysis.

Specimen ID	$F_{\max}$	$F_{\max}^{Num}$	$\left\|F_{\max} - F_{\max}^{Num}\right\| / F_{\max}$ (%)
G1-F1.1-S0	240.12	221.04	7.9
G1-F1.1-S23	244.80	249.08	1.74
G1-F1.1-S46	245.6	251.53	2.41
G2-F0	229.52	207.63	9.53
G2-F0-ST	277.98	263.88	5.0
G2-F1.1	263	296.91	12.89
G2-F1.5	293.75	302.78	3.07
		Average	6.07

Table-9 MC2010 [28] and RILEM TC 162-TDF [29] and Soetens [30] approaches for predicting shear resistance of FRC beams.

<table>
<tr><th>Shear approach</th><th>Analytical shear formula</th><th>Parameters</th></tr>
<tr><td>

RILEM TC-162-TDF

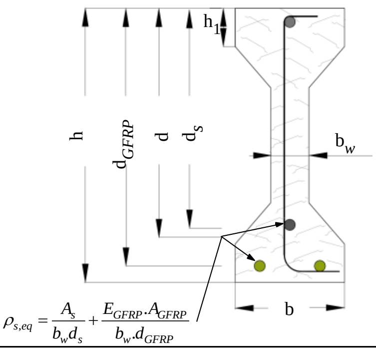

</td><td>

$$V_{cd} = \left[\frac{C_1}{\gamma_c} k^* \, (100\rho_s f_{ck})^{1/3} + 0.15\sigma_{cp}\right] b_w d \quad (10)$$

$$k = 1 + \sqrt{200/d} \leq 2.0 \quad (11)$$

$$V_{fd} = 0.7 k_f^{**} \, k \frac{C_1 f_{R4}}{\gamma_c} b_w d \quad (12)$$

$$k_f = 1 + n.(h_1^{\dagger} / b_w).(h_1 / d) \leq 1.5 \quad (13)$$

$$n = (b^{\dagger\dagger} - b_w) / h_1 \leq 3 \text{ and } n \leq (3b_w / h_1) \quad (14)$$

</td><td>

$C_1 = 0.18$

$\gamma_c = 1$

</td></tr>
<tr><td>

CEB-FIP MC2010

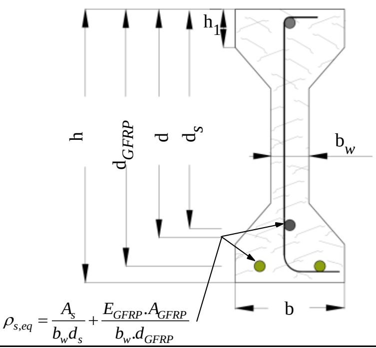

</td><td>

$$V_{Rd,F} = \left[\frac{C_1}{\gamma_c} k(100\rho_s C_2 f_{ck})^{1/3} + 0.15\sigma_{cp}\right] bd \quad (15)$$

$$C_2 = 1 + 7.5 \frac{f_{Ftuk}}{f_{ctk}} \quad (16)$$

$$f_{Ftu} = f_{Fts} - \frac{w_u^{□□}}{CMOD_3}(f_{Fts} - 0.5 f_{R3} + 0.2 f_{R1}) \geq 0 \quad (17)$$

$$f_{Fts} = 0.45 f_{R1} \quad (18)$$

</td><td>

$C_1 = 0.18$

$\gamma_c = 1$

</td></tr>
<tr><td>

Soetens 2015

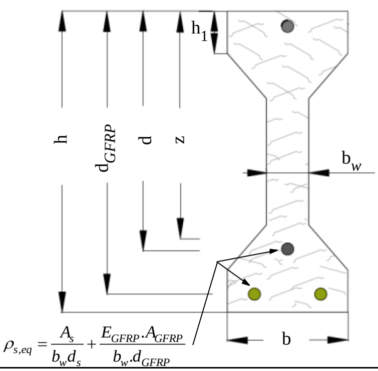

</td><td>

$$V_{Soetens2015} = \left[0.388\sqrt{1+\frac{\sigma_{cp}}{f_{ck}}} k(3\frac{d}{a}\rho_s)^{1/3}\sqrt{f_{cm}} + f_{Ftu}^{*}(1+4\frac{\sigma_{cp}}{f_{ck}})\right] b_w z^{□} \quad (19)$$

$$z^{□} = 0.9 \times d \quad (20)$$

</td><td></td></tr>
</table>

*k: size effect factor.

** k_f : coefficient corresponding to the effect of the beam flanges.

† h_1 : height of the flange.

†† b : width of the flange.

□ z : Internal lever arm.

□□ w_u : maximum crack opening accepted in structural design.

Table-10 Shear resistance calculated analytically in comparison with the experimental results.

	Specimen ID	$V_{\exp}$ (kN)	v_u (MPa)	V_{MC2010} (kN)	$\frac{V_{\exp}}{V_{MC2010}}$	V_{RILEM} (kN)	$\frac{V_{\exp}}{V_{RILEM}}$	$V_{Soetens2015}$ (kN)	$\frac{V_{\exp}}{V_{Soetens2015}}$
Group 1	G1-F1.1-S0	120.1	4.1	60.62	1.98	135.8	0.88	139.01	0.86
	G1-F1.1-S23	122.4	4.2	67.65	1.81	142.8	0.86	151.24	0.81
	G1-F1.1-S46	122.8	4.2	74.70	1.64	149.9	0.82	161.35	0.76
Group 2	G2-F0	114.8	3.9	60.67	1.89	60.7	1.89	43.4	2.64
	G2-F0-ST	139.0	4.7	110.85	1.25	110.9	1.25	-	-
	G2-F1.1	131.5	4.5	89.24	1.50	164.4	0.80	175.16	0.74
	G2-F1.5	146.9	5.0	87.77	1.70	176.83	0.83	171.75	0.86
	Average				1.68		1.05		1.11
	CoV (%)				14.77		38.48		67.49